CrossMark

Type Ia Supernova Nucleosynthesis: Metallicity-dependent Yields

James D. Keegans[1,2,12] , Marco Pignatari[2,3,4,5,12] , Richard J. Stancliffe[2,6,12] , Claudia Travaglio[7], Samuel Jones[8] ,
Brad K. Gibson[2] , Dean M. Townsley[9] , Broxton J. Miles[10] , Ken J. Shen[11] , and Gareth Few[2]

[1] Astrophysics Group, Lennard-Jones Laboratories, Keele University, Keele ST5 5BG, UK; j.d.k.keegans@keele.ac.uk
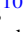[2] E.A. Milne Centre for Astrophysics, University of Hull, Hull HU6 7RX, UK
[3] Konkoly Observatory, Research Centre for Astronomy and Earth Sciences, Hungarian Academy of Sciences, Konkoly Thege Miklos ut 15-17, H-1121 Budapest, Hungary
[4] CSFK, MTA Centre of Excellence, Budapest, Konkoly Thege Miklós út 15-17, H-1121, Hungary
[5] Joint Institute for Nuclear Astrophysics—Center for the Evolution of the Elements, USA
[6] H.H. Wills Physics Laboratory, University of Bristol, Tyndall Avenue, Bristol BS8 1TL, UK
[7] INAF-Astrophysical Observatory, Turin, Italy
[8] Theoretical Division, Los Alamos National Laboratory, Los Alamos, NM 87545, USA
[9] Department of Physics and Astronomy, University of Alabama, Tuscaloosa, AL, USA
[10] Applied Research Associates, Inc., Raleigh, NC, USA
[11] Department of Astronomy and Theoretical Astrophysics Center, University of California, Berkeley, CA 94720, USA

Abstract

Type Ia supernova explosions (SN Ia) are fundamental sources of elements for the chemical evolution of galaxies. They efficiently produce intermediate-mass (with Z between 11 and 20) and iron group elements—for example, about 70% of the solar iron is expected to be made by SN Ia. In this work, we calculate complete abundance yields for 39 models of SN Ia explosions, based on three progenitors—a 1.4 $M_\odot$ deflagration detonation model, a 1.0 $M_\odot$ double detonation model, and a 0.8 $M_\odot$ double detonation model—and 13 metallicities, with ^{22}Ne mass fractions of 0, 1×10^{-7}, 1×10^{-6}, 1×10^{-5}, 1×10^{-4}, 1×10^{-3}, 2×10^{-3}, 5×10^{-3}, 1×10^{-2}, 1.4×10^{-2}, 5×10^{-2}, and 0.1, respectively. Nucleosynthesis calculations are done using the NuGrid suite of codes, using a consistent nuclear reaction network between the models. Complete tables with yields and production factors are provided online at Zenodo:Yields (https://doi.org/10.5281/zenodo.8060323). We discuss the main properties of our yields in light of the present understanding of SN Ia nucleosynthesis, depending on different progenitor mass and composition. Finally, we compare our results with a number of relevant models from the literature.

Unified Astronomy Thesaurus concepts: Type Ia supernovae (1728); Nucleosynthesis (1131); Astrophysical explosive burning (100); Nuclear astrophysics (1129)

1. Introduction

Type Ia supernovae (SN Ia) are explosions ignited from electron degenerate carbon–oxygen (CO) white dwarf (WD) progenitors. Thermonuclear detonation of degenerate CO cores can generally reproduce the main features of SN Ia explosions. Among other features, they reproduce the SN light-curve luminosities observed, the characteristics of the Philips relationship, and they efficiently produce iron group elements as required from galactic chemical evolution (GCE) simulations (see, for example, Sim et al. 2010; Nomoto & Leung 2017, 2018; Gronow et al. 2020; Matteucci 2021). However, the dominant mechanisms driving the SN Ia explosions remain uncertain. The explosion may be the outcome of mass transfer in either a single degenerate (one compact object) or double degenerate (two compact objects) system, and for each of these cases, the compact object accreting material may explode either near the Chandrasekhar mass in a deflagration to detonation transition, or as a sub-Chandrasekhar double detonation. Livio & Mazzali (2018) presented a comprehensive review of the possible pathways to

explosion for SN Ia describing these and other pathways to explosion.

As WDs are unconditionally stable as isolated objects, a companion star is necessary to initiate the explosion. The nature of the companion influences the nucleosynthesis and ejected yields from the SN Ia. As SN Ia have been used for decades as standardizable candles for extragalactic distance measurements and for GCE modeling, unambiguous identification of the progenitors of SN Ia is crucial to reduce systematic errors of GCE models and improve their predictive abilities (Hillebrandt et al. 2013; Livio & Mazzali 2018).

At present, it is a matter of debate as to the relative contributions of Chandrasekhar and sub-Chandrasekhar-mass progenitors. Based on GCE calculations of [Mn/Fe] in the Milky Way disk and in the solar neighborhood, Seitenzahl et al. (2013a) found that 50% of SN Ia should originate from sub-Chandrasekhar-mass WDs, Scalzo et al. (2014) obtained a range of between 25% and 50%, and Eitner et al. (2020) found about 75%. Late time spectroscopy also favors sub-Chandrasekhar progenitors, with up to 85% of WDs predicted to be of this type (Flörs et al. 2020). In addition to this, there are difficulties in the observation of Mn. Most studies assume local thermal equilibrium (LTE) when calculating abundances; however, Bergemann & Gehren (2008) found that the assumption of LTE for heavier elements can increase the inferred abundance of Mn significantly. Mishenina et al. (2015) confirmed that most Mn is produced by thermonuclear

---

[12] NuGrid Collaboration; http://nugridstars.org.

supernovae, but do not identify a statistical difference between the LTE or non-LTE assumptions.

There also exists tension between the single and double degenerate models of progenitors—Woods & Gilfanov (2014) found that the contribution of single degenerate progenitors can be restricted significantly by considering the upper limits of detection of He II and C II emission lines in UV emission spectra of early-type galaxies. They find from these observations that contributions from the single degenerate scenario should account for less than 10% of observed SN Ia.

There are a number of potential progenitors of SN Ia that are discussed extensively in the literature and are reviewed in, for example, Maoz & Mannucci (2012). They are most commonly split into two categories—the single and the double degenerate scenarios. In the single degenerate scenario, a WD primary accretes material from a main-sequence or helium-burning companion. Depending on the evolutionary pathway of the SN Ia event, the ignition of the WD may occur through several different mechanisms. For example, the primary C/O white dwarf may reach the Chandrasekhar mass or the carbon may be ignited in the core of the WD through a detonation in an accreted helium layer. In addition to these commonly considered scenarios, there are other less favored mechanisms —for a full discussion, see Livio & Mazzali (2018). In the double degenerate model, both the primary and secondary stars are C/O white dwarfs. In this case, the secondary is either disrupted to form an accretion disk or may collide with the primary (Raskin et al. 2010).

The energy generation during the SN Ia explosion is largely insensitive to the choice of nuclear reaction rates. Bravo & Martínez-Pinedo (2012) found there is a variation of less than around 4% in energy generation when varying the ^{12}C ^{12}C or ^{16}O ^{16}O reaction rates by a factor of 10 or 0.1. They also observe a small impact on the abundance of iron group isotopes when a large range of charged particle reactions are varied, although a larger difference is observed in the intermediate-mass region for the same variations in reaction rates. Parikh et al. (2013) performed a sensitivity study on over 2300 reaction rates, and found that only 53 reaction affect the yield of any isotope with an ejected mass of more than $10^{-8}M_\odot$ by more than a factor of 2 when varied by a factor of 10. This further indicates that the nucleosynthesis during the SN Ia explosion is robust in the face of reaction rate changes; however, they did identify some key reaction rates (for example, α capture rates on ^{12}C and ^{20}Ne along with some electron-capture rates), which do impact the isotopic yields of the system. The role of radionuclide production and the impact of reaction rates in the ratios of observable radionuclides is also discussed in Parikh et al. (2013), who found that variations in the ratio of certain radionuclides can be up to a factor of 10 different depending on the choice of reaction rates. This suggests that though the isotopic and elemental yields of SN Ia are largely insensitive to the reaction rates, simulations of the SN Ia light curve may depend more sensitively on the reaction rates chosen. In the more recent study by Bravo (2019), a focus on varying the weak reaction rates during the explosion confirms that weak reaction rate increases cannot lead to production of neutron-rich isotopes in sub-Chandrasekhar-mass progenitors. Fitzpatrick & Shen (2021) also found that the iron group abundances are relatively insensitive to reaction rate uncertainties; however, there are a number of rates identified that impact the abundances of intermediate-mass elements.

While variations in reaction rates are clearly important for investigating the production of some isotopes during the explosion, we do not include such a study in this work.

Each of the various formation channels presents challenges, as none reproduces all of the observational data of a typical SN Ia: double degenerate merger light curves with a total mass larger than the Chandrasekhar mass are too broad (Fryer et al. 2010). However, their calculated rate better matches the observed frequency of SN Ia (Nomoto et al. 1997a) and explains the absence of hydrogen in the spectra (Hillebrandt & Niemeyer 2000). For the case where the double degenerate double detonation occurs before the formation of a remnant— with an explosion mass less than the Chandrasekhar mass— simulated light curves are similar to the sub-Chandrasekhar case. For the single degenerate case, growing the white dwarf mass to the Chandrasekhar mass through accretion is difficult except for a narrow range of accretion rates (Cassisi et al. 1998; Hillebrandt & Niemeyer 2000) although forming a helium shell through accretion is easier, as no stable burning is required. Observed delay time distributions of SN Ia explosions cannot be explained solely by the single degenerate scenario (Mennekens et al. 2010), and require at least a component from the double degenerate model.

In this work, we investigate the Chandrasekhar-mass model of Townsley et al. (2016; T1.4) which undergoes a deflagration to detonation transition, and the two sub-Chandrasekhar models of Shen et al. (2018; S1.0) and Miles et al. (2019; M0.8), which are both pure detonations. We focus in this work on the effect of the progenitor mass, rather than the pathway to explosion, as, while there are a number of important observables governed by the path to explosion such as radio emission from circumstellar material (Kool et al. 2023), gamma-ray observations of radionucleids (Summa et al. 2013), high-velocity features of ejecta (Silverman et al. 2015), early light-curve observations (Hosseinzadeh et al. 2017), and other features (Hillebrandt et al. 2013; Maoz et al. 2014; Livio & Mazzali 2018), the bulk nucleosynthesis in the models investigated here depends on the peak temperature and central density only. Initial mass is not the only parameter that effects the prediction of GCE models, however. Matteucci et al. (2009) showed that the fraction of prompt SN Ia explosion (those occurring in the first 100 Myr) has a larger impact in GCE simulations than the nature of the SN Ia progenitor and whether it is a single or double degenerate model.

Observed isotopic abundances from SN Ia are not readily available—they are widely regarded to not produce grains in their ejecta and so there is no single source isotopic abundance data available for them, other than for ^{55}Mn, as stable Mn is monoisotopic. We can deduce the contribution to the solar budget of various isotopes by eliminating contributions from other stellar sources; however, this limits our predictive power to those isotopes that are dominated by the contribution from SN Ia or that have well-constrained contributions from all other sources. γ-ray spectroscopy presents an alternative probe of the nucleosynthesis in the SN Ia explosions, and therefore, radionuclides with large production differences between models and with appropriate half-lives provide a potential tracer of the explosion conditions of the SN and the progenitors, although this is not discussed in this work.

The main products of SN Ia explosions are in the intermediate-mass elements and in the iron group. Matteucci & Greggio (1986) compared the relative contributions of type I

and II supernovae and found that SN Ia are the bulk producers of iron, producing around 70% of solar iron, and argued for a significant contribution to the elemental abundance of Si of around 42%. SN Ia explosions contribute significantly to the production of the isotopes ^{50,52,54}Cr, ^{55}Mn, ^{54,56,57,58}Fe, ^{59}Co, ^{58,60,61}Ni, and ^{64}Zn, as well as isotopes of Ne, Na, Mg, and Si as discussed in, e.g., Nomoto et al. (1984), Woosley et al. (2002), and Travaglio et al. (2011). Many sources of SN Ia yields are available in the literature, including an extensive suite of postprocessed explosions in the Heidelberg Supernova Model Archive—e.g., Fink et al. (2010), Kromer et al. (2010), Pakmor et al. (2010), Travaglio et al. (2004), and Travaglio et al. (2011), where detailed modeling of the accreted He envelope shows the production of p-nuclei; the yields of Nomoto (1982; W7) and Leung & Nomoto (2018); the yields of Shen et al. (2018); and the 2D yields of Boos et al. (2021)

In this work, we present new nucleosynthesis yields for 39 SN Ia models. We consider three progenitor masses—the 1.4 $M_\odot$ mass deflagration detonation model of Townsley et al. (2016; T1.4), the 1.0 $M_\odot$ double detonation model of (Shen et al. 2018; S1.0), and the 0.8 $M_\odot$ double detonation model of (Miles et al. 2019; M0.8). By varying the ^{22}Ne initial abundance, we provide the yields for 13 metallicities for each progenitor, between $Z_{met} = 0$ and $Z_{met} = 0.1$. A large number of different SN Ia yield prescriptions have been used for GCE simulations in the literature, depending on the type of analysis and on the main research area. For example, Mishenina et al. (2017) compared GCE calculations with the Milky Way disk stars using four different codes. They adopted different SN Ia yields and different implementations for them with respect to metallicity, but they were all based on Chandrasekhar-mass progenitors only. More recently, the same approach was used by Prantzos et al. (2018). Kobayashi et al. (2020a) performed GCE studies using two SN Ia progenitors and metallicities spanning from $Z_{met} = 0$–0.1. The models presented in this work are therefore aligned with current GCE modeling, although yields from more progenitor systems may be necessary in specific works that use a larger number of progenitor models for their investigations (see, for example, Lach et al. 2020; Gronow et al. 2021). Note also that the 0.8 M_{Sun} presented in this work is not expected to resemble a typical SN Ia and may be too dim to be observed; it may therefore not be suitable for GCE studies, but has been included here as a limiting case.

2. Nucleosynthesis Models and Stellar Simulations

2.1. Tppnp: Parallelized Postprocessing

The postprocessing nucleosynthesis calculations presented in this work are completed using the NuGrid code tppnp: tracer particle postprocessing network-parallel. A full description of the tppnp code can be found in Jones et al. (2019b), along with details about the nuclear reaction network in Ritter et al. (2018) and Pignatari et al. (2016). Key improvements implemented in Jones et al. (2019b) include the introduction of a variable-order semi-implicit integrator (the Bader-Deuflhard method; Bader & Deuflhard 1983; Deuflhard 1983; Timmes 1999), and nuclear statistical equilibrium (NSE) state solutions are coupled with weak reaction rates using an integration method outlined in Cash & Karp (1990; Cash–Karp Runge–Kutta). The NSE solver is consistent with the full reaction network, and a treatment of electron screening

taken from Chugunov et al. (2007) is implemented. Our reaction network consists of over 5200 isotopes and over 75,000 reactions. After the postprocessing of tracer particles, all radioactive products are allowed to fully decay to stability before the final yields are presented.

The sets of trajectories T1.4, S1.0, and M0.8 are based on hydrodynamics simulations using more limited networks. We find in this work that those networks in Townsley et al. (2016), Shen et al. (2018), and Miles et al. (2019) are sufficient to capture the broad nucleosynthesis in these models. However, for some isotopes, our results differ by more than a factor of 2–3 (see Section 5 for a full discussion thanks to the change in reaction network). The network used in the postprocessing of T1.4 uses 225 nuclides in the reconstruction of the thin flame front (Townsley et al. 2016). These include weak reactions discussed in Calder et al. (2007), which are necessary for the computation of the neutronization in the flame front and are taken from Langanke & Martínez-Pinedo (2000) and Langanke & Martínez-Pinedo (2001). Where newer rates are not available, they use those found in Fuller et al. (1985) and Oda et al. (1994). The standard TORCH network is extended in their work, including 25 additional reactions pertaining to neutron-rich Fe-group isotopes. We also see production of trace amounts of higher-Z material not found in Townsley et al. (2016) because of our more extended network, with total ejected mass of the order of $10^{-9}\ M_\odot$. The network in Shen et al. (2018) used for the hydrodynamical modeling consists of 41 isotopes and 190 reactions, all of which were taken from the JINA reaclib library (Cyburt et al. 2010). With errors of only a few percent in energy generation, they find that this network is sufficient to follow the explosion dynamics. Postprocessing in this work was carried out with a 205 isotope network using MESA (Paxton et al. 2010), again with all reactions being taken from JINA reaclib. Finally, the network in Miles et al. (2019) is again 205 isotopes, also with JINA reaclib rates. In each case, the hydrodynamics have been calculated separately, with the final yields being postprocessed.

Variations arise from a difference in the choice of reaction rates used between the NuGrid postprocessing codes and those used in the original publications. Postprocessing these models again with a consistent nuclear reaction network between them allows us to disentangle the nuclear physics uncertainties from hydrodynamical modeling uncertainties.

Reaction rates for the tppnp code are taken from a variety of different sources: the Rauscher & Thielemann (2000) JINA reaclib, Cyburt et al. (2010) Basel reaclib, Dillmann et al. (2006) KADoNiS, Caughlan & Fowler (1988), Angulo et al. (1999) and Iliadis et al. (2001); note that compilations between them constitute the majority of reactions other than the weak reaction rates, which are compiled from Fuller et al. (1985), Oda et al. (1994), Goriely (1999), and Langanke & Martínez-Pinedo (2000), along with rates from Takahashi & Yokoi (1987) as discussed in Jones et al. (2019b) and Pignatari et al. (2016). The NSE solver is based on the theory described in Seitenzahl et al. (2008), and care was taken to include coulomb screening and ensure consistency between the reaction network and NSE solution as has been described by Calder et al. (2007).

Following a common approach in the literature, we select an initial abundance of metals determined by the mass fraction of ^{22}Ne. ^{22}Ne acts as a proxy for the metallicity of the progenitor in this work, as the weak interaction ^{18}F$(\beta^+)^{18}$O in the CNO cycle converts protons to neutrons and changes the electron

Table 1
Number of Particles, Maximum Peak Temperature, and Number of Time Steps
for Each of the Three Classes of Model Investigated in This Work

Parameter	T1.4	S1.0	M0.8
No. of Particles Postprocessed	7856	107	9996
T_{peak} Max (GK)	10.28	6.32	5.21
No. Time Steps	6872	58738	1347

fraction of the system. The electron fraction can also change through carbon simmering or freeze-out from neutron-rich NSE (Martínez-Rodríguez et al. 2017) in near-Chandrasekhar-mass progenitors.

The initial composition, beyond the electron fraction, is not important in those particles that reach NSE, and the composition of the outer, cooler layers of the white dwarf is unlikely to resemble scaled solar abundances. We have therefore chosen to treat our white dwarf as having neutron excess only in the form of ^{22}Ne.

We note that the parent model for the S1.0 case does not include an accreted helium layer from a companion star, and the detonation is ignited centrally. Shen et al. (2018) presented the limiting case for the explosion where the accreted helium shell is minimally thin, and as such the conditions of the S1.0 case are representative of a single detonation scenario. Without the helium ashes of this accreted shell, the ejected abundances fail to take into account possible p-nuclei production, as discussed in Travaglio et al. (2005), as well as an increase in the ejected abundances of some key iron group isotopes as discussed in, for example, Magee et al. (2021).

T1.4 chose a scaled solar abundance for their models, except for the CNO material, which was treated the same as ^{22}Ne as in Timmes et al. (2003), with a constant abundance throughout the WD. The rest of the material is composed of C and O, and convective burning ashes: ^{20}Ne, ^{16}O, ^{13}C, and ^{22}Ne. S1.0 included ^{22}Ne and ^{56}Fe as proxies for the abundances of non-C/O isotopes and as a tracer of metallicity, again with a uniform distribution of abundances in the WD. M0.8 used solar abundances taken from Asplund et al. (2009).

Table 1 shows some of the key parameters of each of the three models investigated in this work; namely the number of postprocessed tracer particles, the maximum peak temperature of any particle in that set of tracer particles, and the number of time steps in each trajectory. M0.8 has the greatest number of particles, with approximately 10^4 being extracted for the postprocessing step. We have extracted a similar number of particles from the T1.4 model, after performing a convergence study to ensure that our results were consistent with the full 10^5 particles of the T1.4 model. This was achieved by running the full particle set and comparing with yields from reduced numbers of particles selected from every 10th, 15th, 20th, and 100th particle in the data set. Convergence of our results was seen for the case where 1 in 10 particles was selected. S1.0 has only 107 tracers in the parent model; however, Shen et al. (2018) showed that this is sufficient to model the SN Ia explosion. Due to the sparse nature of the S1.0 tracer particles, many of the diagnostic plots presented later in this work appear to have missing data, but this is an artifact of the smaller number of tracers in the S1.0 models.

Time resolution in the three models varies significantly. The S1.0 model is highly resolved, with close to 6×10^5 time steps. In this case, the trajectories remain as they were when extracted

from the hydrodynamical modeling. This is in order to not introduce inconsistencies in the yields with respect to those published for S1.0. The number of time steps for the M0.8 and T1.4 models is comparable, at around 10^3 per trajectory.

For the T1.4 model, resolution in mass in the hotter parts of the explosion is high; however, the resolution in the outer layers of the WD is not as high as that found in Travaglio et al. (2004). For instance, we can make no predictions about the abundances of p-nuclei in any of our models as the CO WDs of the S1.0 and M0.8 models are treated as having a minimally thin accreted He shell (i.e., no shell). The production of p-nuclei as described in Travaglio et al. (2015) depends sensitively on the nucleosynthesis during the He shell flashes and on the heavy element abundances, which are built during the accretion phase. They subsequently form the seeds of the p-process activated during the supernova explosion (Battino et al. 2020). Without this component, our calculations do not include p-process yields.

In the models of Townsley et al. (2016), based on the earlier work of Calder et al. (2007) and Townsley et al. (2007), the explosion in the WD progenitor is initiated through the introduction of an artificial hot spot at a predetermined radius. In Townsley et al. (2016), there are a number of important improvements to the original models, including the ability to change the Y_e of the fuel. The most notable feature of the Townsley et al. (2016) models, however, is the introduction of reconstruction of the trajectories. The flame front during the SN Ia explosion is artificially thick in the raw data from the hydrodynamic modeling. In order to account for this, the reconstruction process narrows the flame by reducing the effective time that the material spends at the peak temperatures in the simulation.

The S1.0 models utilize the FLASH code (Fryxell et al. 2000) in order to model 1D explosion, using density profiles from MESA for the initial conditions of their WD progenitor. The explosion in this model is also initialized by a hot spot, here with a central temperature of 2 GK. The hotspot is relatively large compared to the minimum detonatable region; however, the mass of the spot is small. Shen et al. (2018) argued that this also therefore minimizes the impact on the ejected yields. The M0.8 model uses a uniform composition throughout the WD progenitor, with 1.4% of metals. The ignition of this model is again achieved with the introduction of a hot spot, this time at 1.98 GK. FLASH is used to evolve the system, through the initial detonation, leading to the triggering of the C/O detonation.

3. SN Ia Yields

The full list of models is shown in Table 2. For each of the three model configurations, a set of 13 metallicities is considered, providing a total of 39 distributions of SN Ia yields. In general, we can identify three broad burning regimes in SN Ia ejecta, similar to explosive burning conditions in massive stars, as discussed in Iliadis (2015). The high-temperature component of these models, with SN temperature peaks on the order of or above 7 GK, are present only in the Chandrasekhar-mass explosions. This is characterized by an efficient production of iron-group material, formed by the freeze-out from NSE. The intermediate component, with peak temperatures between 4.5 and 7 GK, is present in all models. However, the M0.8 suite of yields has a smaller contribution from this region. Production in this peak temperature range

Table 2
List of SN Ia Model Sets Presented in This Work

T1.4Z0	S1.0Z0	M0.8Z0
T1.4Z0.0000001	S1.0Z0.0000001	M0.8Z0.0000001
T1.4Z0.000001	S1.0Z0.000001	M0.8Z0.000001
T1.4Z0.00001	S1.0Z0.00001	M0.8Z0.00001
T1.4Z0.0001	S1.0Z0.0001	M0.8Z0.0001
T1.4Z0.001	S1.0Z0.001	M0.8Z0.001
T1.4Z0.002	S1.0Z0.002	M0.8Z0.002
T1.4Z0.005	S1.0Z0.005	M0.8Z0.005
T1.4Z0.014	S1.0Z0.014	M0.8Z0.014
T1.4Z0.01	S1.0Z0.01	M0.8Z0.01
T1.4Z0.02	S1.0Z0.02	M0.8Z0.02
T1.4Z0.05	S1.0Z0.05	M0.8Z0.05
T1.4Z0.1	S1.0Z0.1	M0.8Z0.1

Note. Models are labeled according to the initial mass of the progenitor and the metallicity. T1.4 corresponds to the Townsley et al. (2016) 1.4 $M_\odot$ deflagration detonation model, S1.0 to the Shen et al. (2018) 1.0 $M_\odot$ double detonation model, and M0.8 to the Miles et al. (2019) 0.8 $M_\odot$ model. Metallicities range from $Z_{met} = 0$ to $Z_{met} = 0.1$, with the initial fraction of metals being represented by the mass fraction of ^{22}Ne with a uniform distribution through all tracer particles.

gives rise to burning products that resemble incomplete explosive silicon burning (Iliadis 2015).

Due to the lower peak temperature range in the M0.8 models and the subsequent small contribution to iron group material, the mass of ^{56}Ni ejected by the M0.8 models is lower when compared to the S1.0 and T1.4 models by orders of magnitude, and a typical SN Ia explosion is not expected from these progenitors.

Absolute yields and production factors for the three model sets, T1.4, S1.0, and M0.8 at all metallicities, are provided for isotopes between C ($Z = 6$) and As ($Z = 33$) as supplementary material. The isotopic production factors for models T1.4Z0, T1.4Z0.014, and T1.4Z0.1 are shown in Figure 1. As expected, large overproductions in the iron group mass region and for the most abundant isotopes of the α-elements Si, S, Ca, and Ti (i.e., ^{28}Si, ^{32}S, ^{40}Ca, and ^{48}Ti) are present at all metallicities. Isotopic production of odd-Z elements and neutron-rich isotopes for light and intermediate-mass even-Z elements increases with increasing metallicity in the SN Ia progenitor.

The large peak in production in the iron group arises from the complete destruction of the ^{12}C and ^{16}O nuclei to α particles, and their subsequent recombination as the temperature drops. For a given Z in the low- to intermediate-mass isotopes ($A \lesssim 45$), the lightest stable nucleus of that element is the most overproduced at low metallicities. As the metallicity of the system increases, we see a boost in production of the heavier isotopes of a given element due to the decreasing Y_e. The bulk of the iron group material is formed in the freeze-out from NSE, at high central densities. These high-density regions modify the Y_e of the material undergoing nucleosynthesis through electron-capture reactions, resulting in a less-pronounced dependence on the initial metallicity of the progenitor (e.g., Brachwitz et al. 2000); however, contributions in the less-dense outer regions of the SN Ia explosion still depend on the initial metallicity of the progenitor.

In particular, as described in Brachwitz et al. (2000), odd–odd nuclei (e.g., ^{40}K) and odd–A (e.g., ^{55}Co, ^{55}Fe) nuclei have the largest effect on the Y_e of the SN Ia explosion. The choice of electron-capture reactions for these nuclei in particular are therefore relevant for nucleosynthesis calculations. Our weak rates are taken from Langanke & Martınez-Pinedo (2000) and Langanke & Martínez-Pinedo (2001). Gamow–Teller back resonances in astrophysical conditions significantly boost electron-capture rates (Brachwitz et al. 2000). Due to the dense conditions in the SN Ia explosion, forbidden transitions are negligible and these resonances dominate (Fuller et al. 1982). In addition to this, Fuller et al. (1982) also highlighted the importance of the neutron closed shells in SN Ia nucleosynthesis, which block further electron captures.

The middle panel of Figure 1 illustrates the effect of the decreased Y_e in this model compared to the analogous model at $Z_{met} = 0$. In particular, through the span of our models, we range from an initial Y_e of 0.5 at $Z_{met} = 0$, to a value of Y_e of 0.495 at $Z_{met} = 0.1$. We see a significant boost in the production of more neutron-rich isotopes in the $A \lesssim 65$ region, with production of, for example, ^{50}Cr, ^{58}Fe, and ^{64}Ni increasing by several orders of magnitude. The odd–even effect is more pronounced in the T1.4Z0.1 run, and the nucleosynthesis shifts in all regions to more neutron-rich isotopes, due to the decreased Y_e.

Comparing Figures 1 and 2, the abundance distribution of the T1.4 and the S1.0 sets of models are similar at all metallicities. For the iron group, the most abundant isotopes of a given element are produced in similar proportions in the two sets of models, but the neutron-rich isotopes are more produced in the T1.4 model. For instance, ^{64}Ni has a production factor of close to the solar value in the T1.4Z0 model, 17 orders of magnitude larger than the S1.0Z0 model. There are 11 orders of magnitude difference in the ^{58}Fe production factor.

The M0.8 set shows a large reduction in the production of iron group isotopes compared with T1.4 and S1.0 sets (Figure 3). Typical differences are between 0.2 times the abundances of the same isotope between the M0.8 and T1.4 cases; however, for some isotopes—all those more massive than ^{58}Ni—the difference is much larger, with no production of these isotopes outside the higher-temperature regions of the T1.4 and S1.0 models. Iron is also underproduced by more than a factor of 15 across all isotopes heavier than ^{54}Fe. Instead, the production of intermediate-mass elements like Si and S and their isotopes is enhanced compared to the heavier models.

4. Yields Analysis by Element

In this section, we describe the production of each stable isotope produced in the SN Ia explosion. We select for elements that have been identified in the literature to have a significant contribution from SN Ia. We primarily use the following publications to identify these elements: Woosley et al. (2002), Pignatari et al. (2016), and Kobayashi et al. (2020a). However, other references are given on an element-by-element basis. All other isotopic abundances are available in the yield tables provided as supplementary material. It should be noted that some isotopes may have a larger contribution from SN Ia where the elemental contribution is negligible; however, these are not discussed in this current work. Where the percentage of an isotope as a fraction of the solar abundance of the element is presented, the data has been taken from the NNDC NuDat 3.0 website (Kinsey et al. 1997, https://www.nndc.bnl.gov/nudat3/).
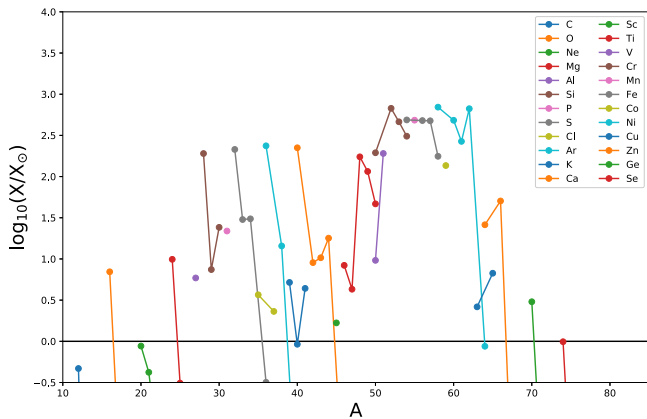
For each set of models, we discuss isotopic yields at metallicities corresponding to mass fractions of ^{22}Ne of 0, 0.014, and 0.1. The figures with the detailed yield distributions in the SN Ia ejecta at these three representative metallicities, including the detailed
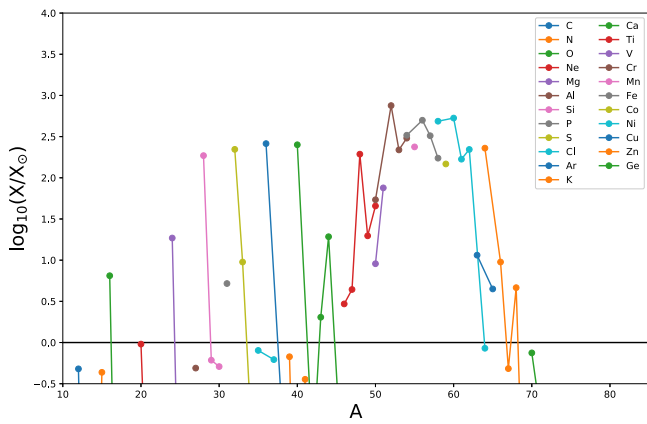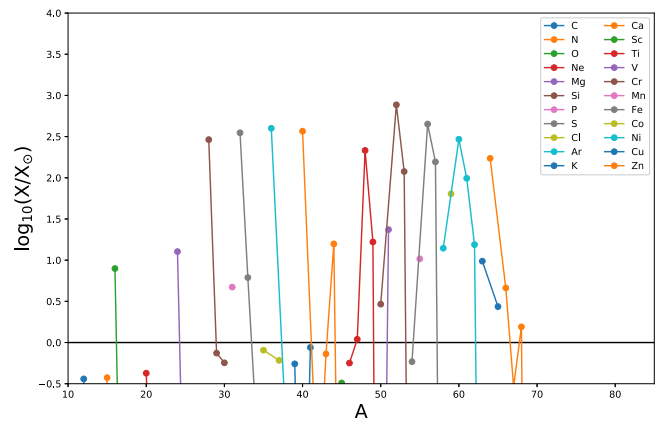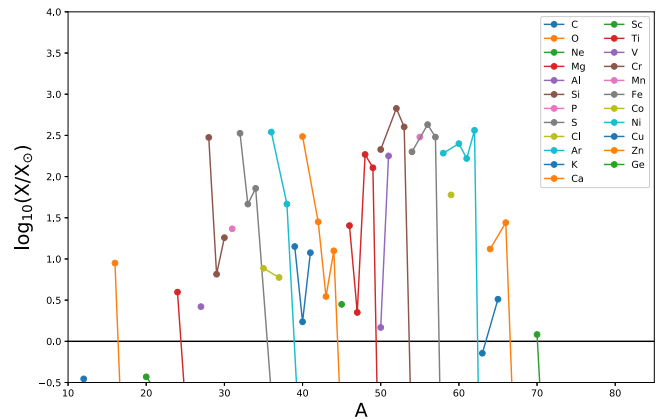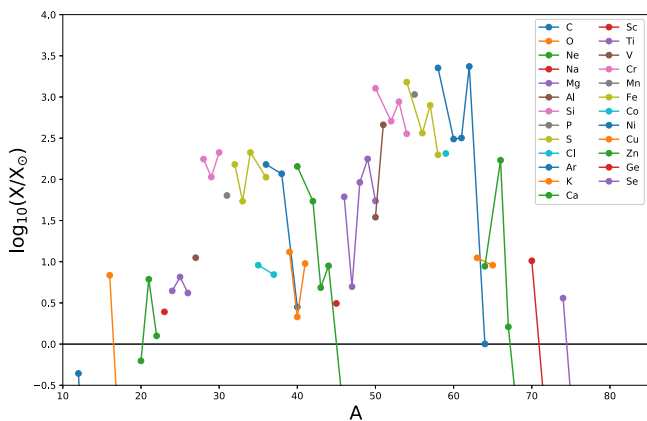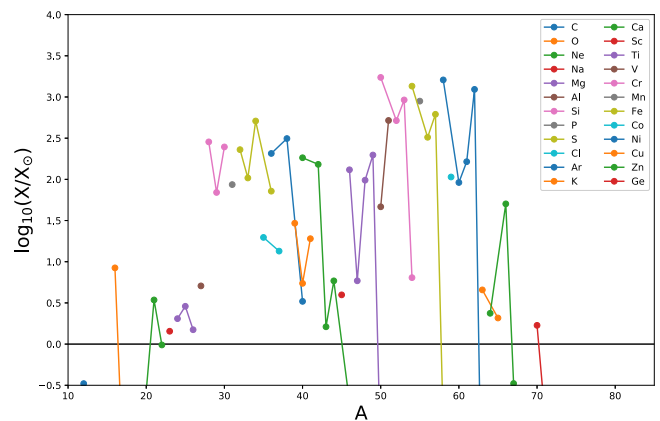
Figure 1. Production factors for models T1.4Z0 (top), T1.4Z0.014 (middle), and T1.4Z0.1 (bottom).

Figure 2. Isotopic production factors for models S1.0Z0, S1.0Z0.014, and S1.0Z0.1.

radiogenic contribution from their parent radioactive species, and for all other isotopes not discussed in the text, are available at Zenodo:Figures (doi:10.5281/zenodo.8059974).

4.1. Silicon

Silicon consists of three stable isotopes: ^{28}Si, ^{29}Si, and ^{30}Si. These are mostly made in core-collapse supernovae (CCSNe); however, contributions from SN Ia events are needed to fit the observed solar system abundances (see, for example,

Seitenzahl et al. 2013b; Kobayashi et al. 2020a). ^{28}Si is the most abundant naturally occurring stable Si isotope (92% of the solar abundance), and is a product of oxygen fusion through the reaction ^{16}O(^{16}O, α)^{28}Si. ^{29}Si is the next most abundant at 4.7%, and ^{30}Si at 3.1%.

In Figure 4, for all models, Si is produced with ejected masses above 0.2–0.3 $M_\odot$. The largest producers of Si are the M0.8 models, with a factor of around 2 larger ejected mass than compared with the other two sets of SN Ia yields across all metallicities. ^{28}Si has no trend with metallicity below the
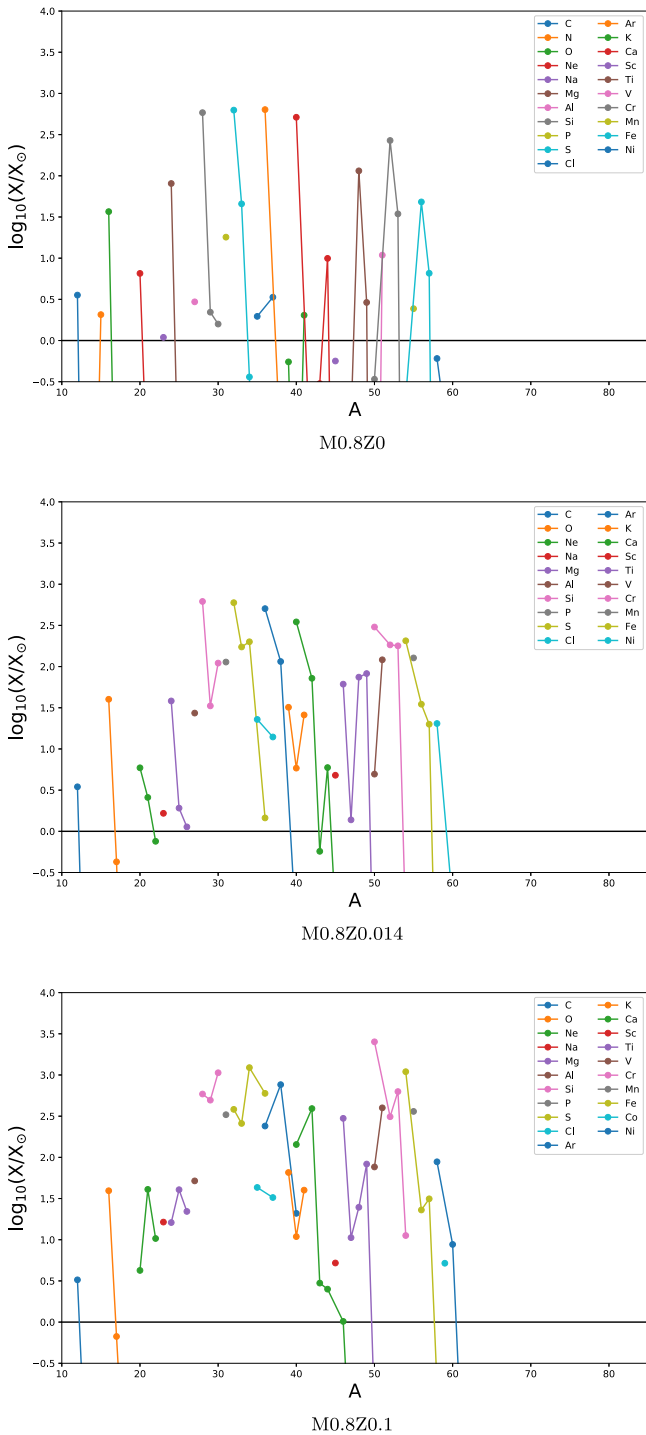
Figure 3. Production factors for models M0.8Z0, M0.8Z0.014, and M0.8Z0.1.
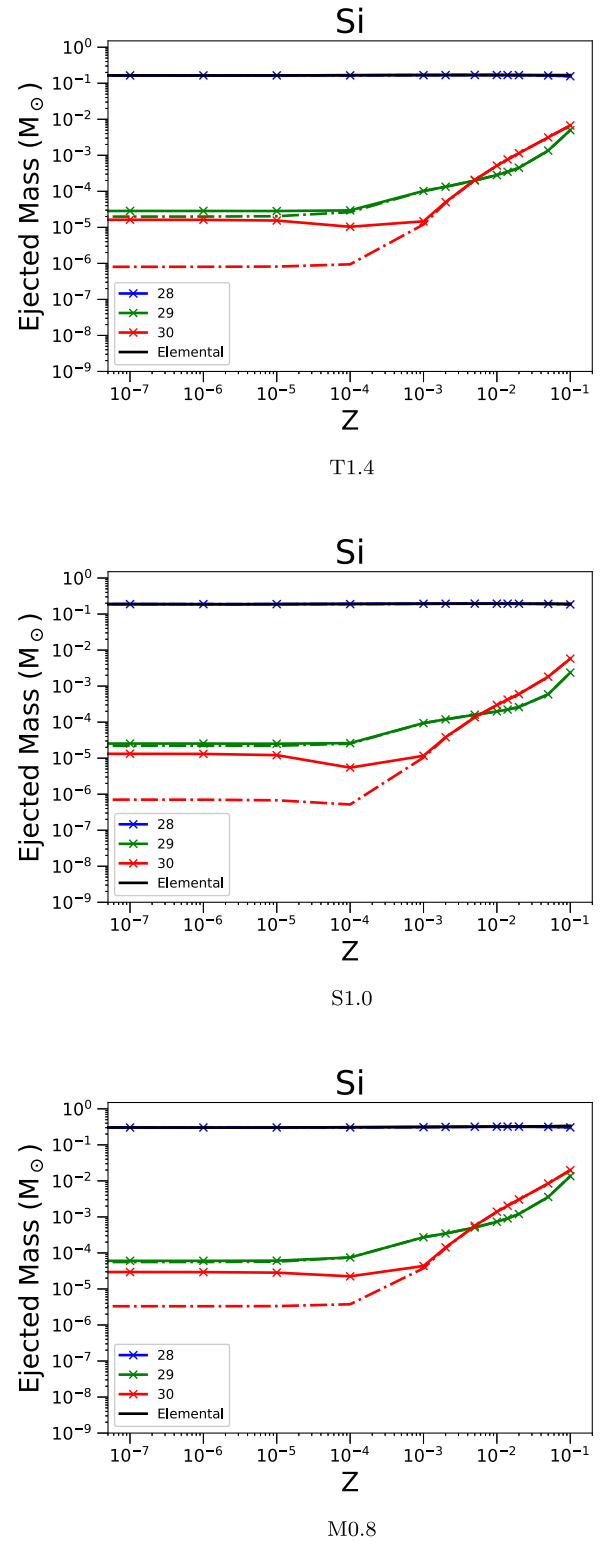

Figure 4. The ejected mass for Si and its stable isotopes ^{28}Si, ^{29}Si, and ^{30}Si are shown at different metallicities. The radiogenic contributions are included in the elemental yields. Decayed and undecayed abundances are shown for isotopes (continuous lines with crosses and dotted–dashed lines with empty circles, respectively). Data is presented for sets T1.4 (upper panel), S1.0 (middle panel), and M0.8 (lower panel).

supersolar-metallicity models. For those, we obtain a small dip in production of all classes of model, arising from reduced production of ^{28}Si at the lowest peak temperatures due to neutron captures. The ^{29}Si and ^{30}Si yields strongly depend on the initial metallicity of the SN Ia progenitors; however, since these isotopes contribute less than 10% of the ejected silicon, they do not affect the overall elemental abundance trend.

The ejected abundance distribution for ^{28}Si is shown in detail for three representative metallicities in Figure 5. All other such isotopic production plots are available on Zenodo:Figures (doi:10.5281/zenodo.8059974), and their features discussed

below. For each model, all tracer particles are plotted without binning of the data.

^{28}Si shows a broad peak of production in all models, stretching from 1.8–6 GK (slightly lower in the S1.0 and M0.8
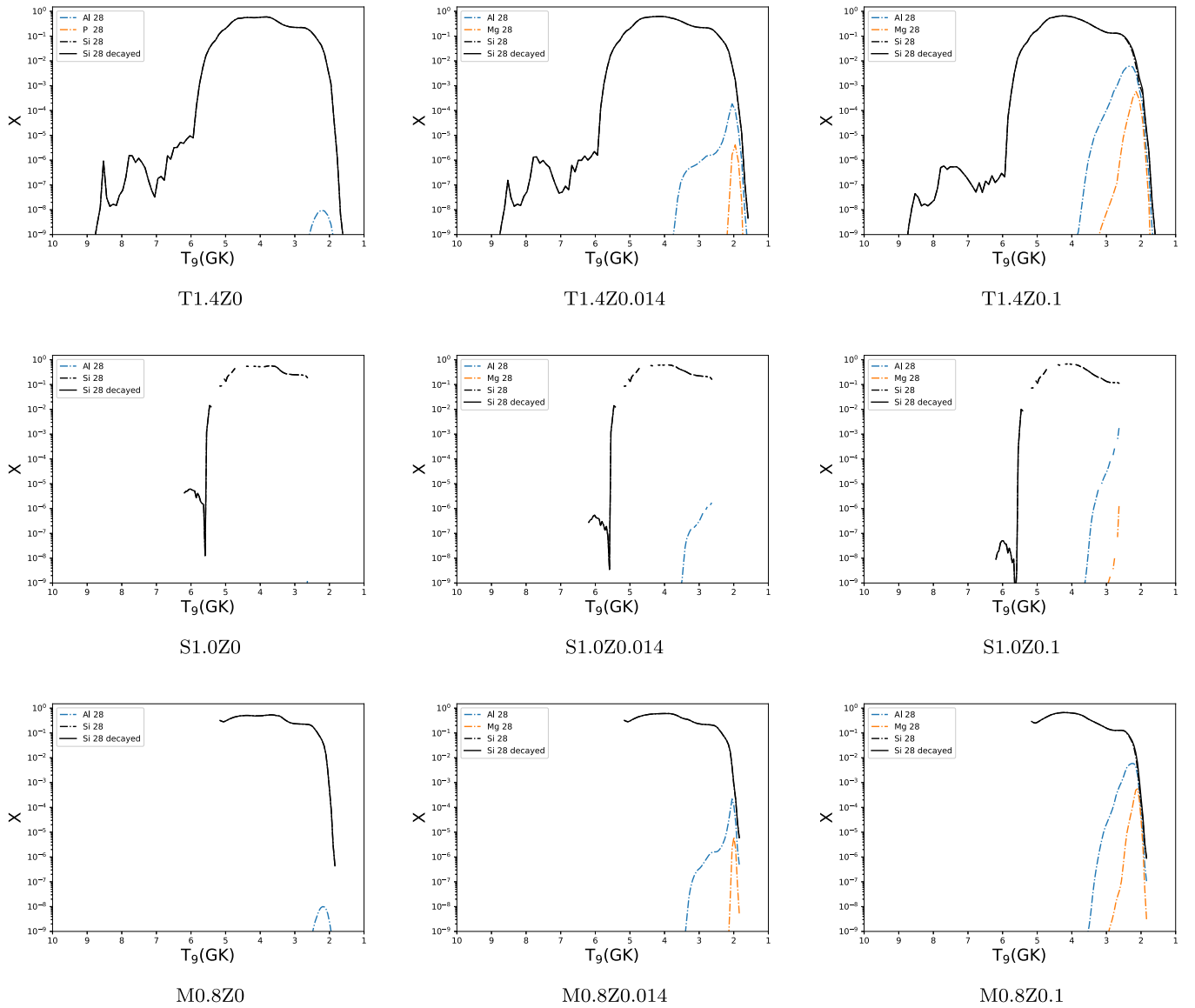
Figure 5. Top panels: the ^{28}Si abundances in the ejecta are shown with respect to the explosion temperature peak (continuous black line) for the models T1.4Z0 ($Z_{met} = 0$, left), T1.4Z0.014 ($Z_{met} = 0.014$, middle), and T1.4Z0.1 ($Z_{met} = 0.1$, right). ^{28}Si abundances are shown with contributions from radioactive species, which are negligible in this case. Middle panels: the same as for top panels, but for models S1.0Z0, S1.0Z0.014, and S1.0Z0.1, respectively. Bottom panels: the same as for top panels, but for models M0.8Z0, M0.8Z0.014, and M0.8Z0.1, respectively.

models, due to the lower density of these tracer particles). Production of ^{28}Si is dominated by direct production: radiogenic contributions are negligible.

Starting in the deepest ejecta (Figure 5), models T1.4Z0, T1.4Z0.014, and T1.4Z0.1 have a smaller production peak at higher temperatures, which is relatively insensitive to the initial metallicity. This is due to the high-density region in the SN Ia causing electron-capture reactions. For stellar conditions where nuclear reaction rates are approaching NSE, charged particle reaction rates are in equilibrium. Therefore, the weak interactions govern the shift in distribution from normal NSE to a more neutron-rich distribution (Langanke & Martınez-Pinedo 2000). The density of these hottest particles ensures that the Y_e is similar between all T1.4 models in the high-temperature region. On the other hand, for all models, the bulk of the ejected ^{28}Si comes from trajectories at lower peak temperatures, and this high-temperature region makes a negligible contribution.

^{29}Si is produced for a broad range of conditions in T1.4Z0, up to 6 GK. Such a small component to the ejected ^{29}Si is not present at higher metallicities, as production moves to more neutron-rich isotopes, where the secondary production at lower peak temperatures instead dominates the isotopic yields. This same trend is seen in the S1.0 and M0.8 models, with a reduction in the production at intermediate peak temperatures accompanied by a boost in production at lower temperatures. The radiogenic ^{29}P abundance is a significant contributor to ^{29}Si in the zero-metallicity models T1.4Z0, S1.0Z0, and M0.8Z0. On the other hand, there is no significant ^{29}P radiogenic contribution for higher metallicities. Only at supersolar metallicities do we see a small contribution to the ejected ^{29}Si mass of the order of a few percent.

The production of ^{30}Si is more complex than ^{29}Si, especially for model T1.4Z0. In this case, broad radiogenic contributions are obtained from two isotopes: ^{30}P is dominant at most peak temperatures, while there is equal production of ^{30}P and ^{30}S at

temperatures above 5 GK. At higher metallicities, for all models, the radiogenic contribution becomes negligible, and most ^{30}Si is ejected directly with a dominant contribution between 2 and 4 GK in all models.

4.2. Sulfur

Sulfur consists of four stable isotopes: ^{32}S, ^{33}S, ^{34}S, and ^{36}S. ^{32}S (the most abundant S isotope in the solar system comprising 94.99% of the solar budget of sulfur) and ^{34}S (4.25% of the solar budget of sulfur) are mostly produced in explosive and hydrostatic oxygen burning in CCSNe. In addition to this component, ^{33}S (0.75% of the solar budget) is also produced by explosive neon burning (e.g., Woosley et al. 2002). Finally, the isotope ^{36}S (the least abundant S isotope in the solar abundances) is made by the s-process in asymptotic giant branch (AGB) stars (Kahane et al. 2000) and by CCSNe, in either hydrostatic helium burning or carbon-oxygen burning (Woosley et al. 2002; Pignatari et al. 2016). Kobayashi et al. (2020a) identified a contribution to the elemental abundance of S from SN Ia.

From Figure 6, the trends of each S isotope are very similar between different sets of model, and show similar trends with respect to metallicity. On the absolute ejected mass of the various S isotopes, the models differ by about a factor of 2 except for ^{33}S, which is more strongly produced in the M0.8 models, at some metallicities by nearly an order of magnitude.

Concerning the detailed production of S species, ^{32}S is directly ejected for all models at low metallicity, with a similar production profile below 5 GK. In the T1.4Z0 model, there is a negligible ^{32}S contribution to the final ejecta from a high peak temperature tail. At solar and supersolar metallicities, we also observe the rise of a secondary production of radiogenic ^{32}S due to the decay of ^{32}P and ^{32}Si. The isotope ^{33}S is mostly made directly in all models. Some contribution is seen from the decay of ^{33}Cl in the models at zero metallicity, and from ^{33}P in solar-metallicity models. The isotope ^{34}S can be made directly in our SN Ia models with a significant contribution from ^{34}Cl at zero metallicity, and from ^{34}P in solar-metallicity conditions. Finally, the ^{36}S abundance ejecta is not shown here as it is negligible, but it is produced directly in all models.

4.3. Argon

Argon consists of three stable isotopes: ^{36}Ar, ^{38}Ar, and ^{40}Ar. ^{36}Ar and ^{38}Ar are produced in CCSNe during oxygen burning and explosive oxygen burning (Woosley et al. 2002). ^{40}Ar (99.6% of the solar Ar budget) is produced either during explosive helium burning by the neutron burst triggered by the supernova shock passage at the bottom of the hydrostatic He shell (Rauscher et al. 2002; Pignatari et al. 2018; Lawson et al. 2022) or by the s-process and then ejected in the convective C-burning shell (e.g., The et al. 2007; Pignatari et al. 2010, 2016). Based on GCE simulations, Kobayashi et al. (2020a) also identified a proportion of elemental Ar as being produced in SN Ia explosions.

In all three sets of models, argon production is mostly primary,[13] with a slight reduction in the total ejected mass at

---

[13] Here, "primary" denotes that material that is synthesized, and its abundance yields do not depend on the initial composition of the stellar SN Ia progenitor. "Secondary" denotes material for which production depends on the seed abundances of other nuclei in the stellar progenitor (ultimately in this work, originating with the initial abundance of ^{22}Ne).

supersolar metallicities (Figure 7). This is due to the decrease in production of ^{36}Ar with increasing metallicity, which is partially compensated for at the highest metallicities with the increase of the ^{38}Ar yields. In the case of the M0.8 models, ^{38}Ar becomes almost as abundant as ^{36}Ar. Indeed, the ratio of ^{36}Ar to ^{38}Ar at supersolar metallicities approaches unity as the mass of the progenitor decreases, while there is a factor of 5 difference in the T1.4Z0.1 model. Radiogenic ^{38}Ar has a primary production up to $Z_{met} = 10^{-4}$, while its direct production drives the increase in yields above $Z_{met} = 10^{-3}$.

For ^{36}Ar, all three classes of models show similar conditions of production and similar trends with metallicity. At $Z_{met} = 0$, ^{36}Ar is primarily produced at temperatures between 4 and 5.5 GK. At temperatures between 2.5 and 3 GK, a small amount of ^{36}Ar is ejected as secondary ^{36}Cl, which remains a small component, even at supersolar metallicities. Overall, the production of ^{36}Ar is not affected by the initial composition of the progenitor.

At zero metallicity, for all of the SN Ia model sets, ^{38}Ar is mainly made as the radiogenic product of ^{38}K, while for solar and supersolar metallicity, ^{38}Ar is directly produced. In the T1.4Z0 model, there is a large ^{38}Ar contribution in the higher temperature range of 5.5–7 GK, temperatures that are not reached in the M0.8 models, and only at the lower end (around 6 GK) in the S1.0 models. ^{38}Ar has an ejected mass approximately five times greater in the low-metallicity models of T1.4 as compared with S1.0 and M0.8 due to this higher-temperature production range. At higher metallicities, the production in the most internal ejecta becomes negligible compared to the metallicity-dependent colder component. The nucleosynthesis in the lower-temperature region is driven by C-fusion and O-fusion.
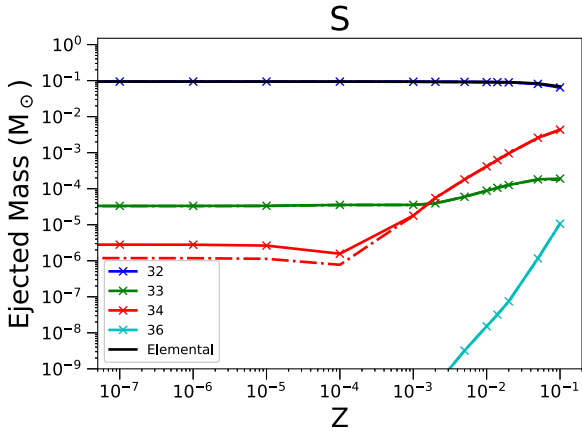
Not shown in these figures, ^{40}Ar does not show any high-temperature component in SN Ia ejecta. The ^{40}Ar production is highly dependent on the initial metallicity, and no models show production of ^{40}Ar at $Z_{met} = 0$. Only trace amounts of ^{40}Ar are synthesized between 2 and 3 GK in the $Z_{met} = 0.014$ models. We instead see a sharp rise in the production of ^{40}Ar at supersolar metallicities (Figure 7).

4.4. Calcium

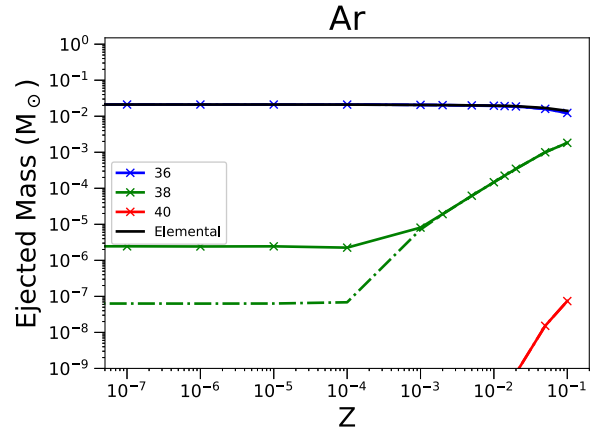Calcium consists of six stable isotopes: ^{40}Ca, ^{42}Ca, ^{43}Ca and ^{44}Ca, ^{46}Ca, and ^{48}Ca. CCSNe provide a significant contribution to the Ca galactic inventory: in these stars, both ^{40}Ca (96.9% of the solar budget) and ^{42}Ca (0.6%) are mostly produced by explosive oxygen burning, and ^{43}Ca (0.1%) is produced in carbon and neon burning, and in α-rich freeze-out following NSE at high temperatures (Woosley et al. 2002). ^{44}Ca (2%) is predicted to be produced efficiently from SN Ia or from α-rich freeze-out in CCSNe, where it is formed as ^{44}Ti (Magkotsios et al. 2010; Pignatari et al. 2016). ^{46}Ca (0.004%) has a contribution from AGB stars, and is also produced in carbon and neon burning in CCSNe. Finally, the origin of ^{48}Ca (0.1%) in nature is unclear, since, in most neutron-rich stellar conditions, it is difficult to produce without overproducing the rare ^{46}Ca. Jones et al. (2019a) showed that, with a small occurrence of thermonuclear electron-capture supernovae, the full solar abundance of ^{48}Ca could be explained. The effective relevance of such a stellar source is however still very uncertain.

For the three sets of models considered here, shown in Figure 8, we obtain similar production trends with metallicity
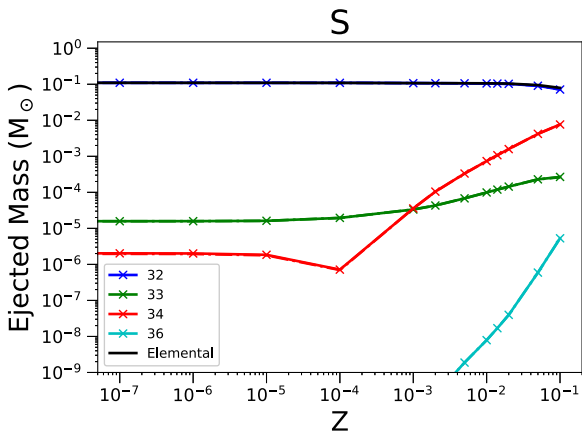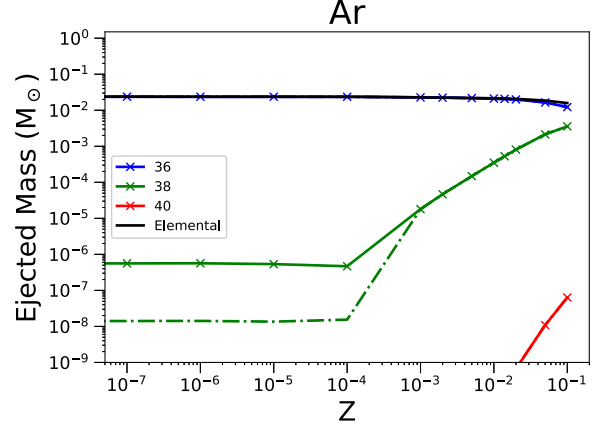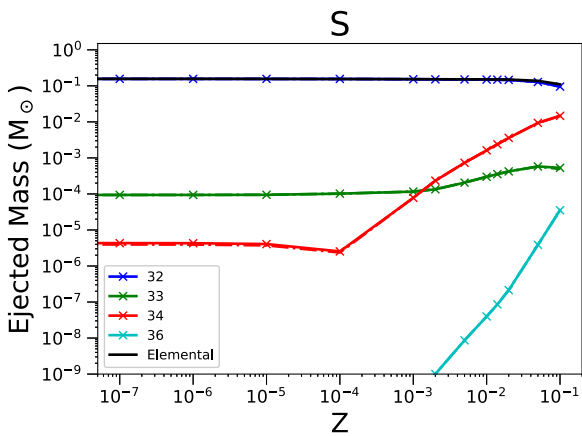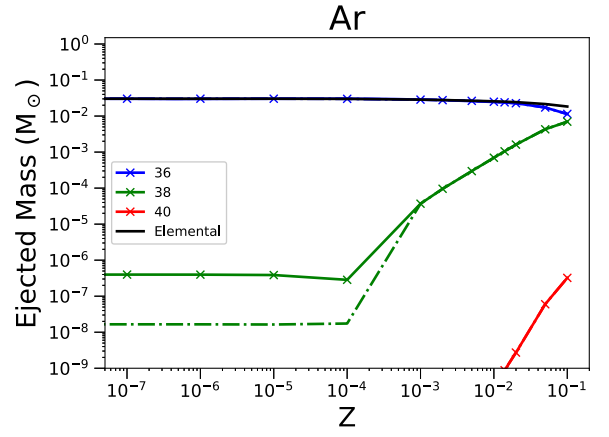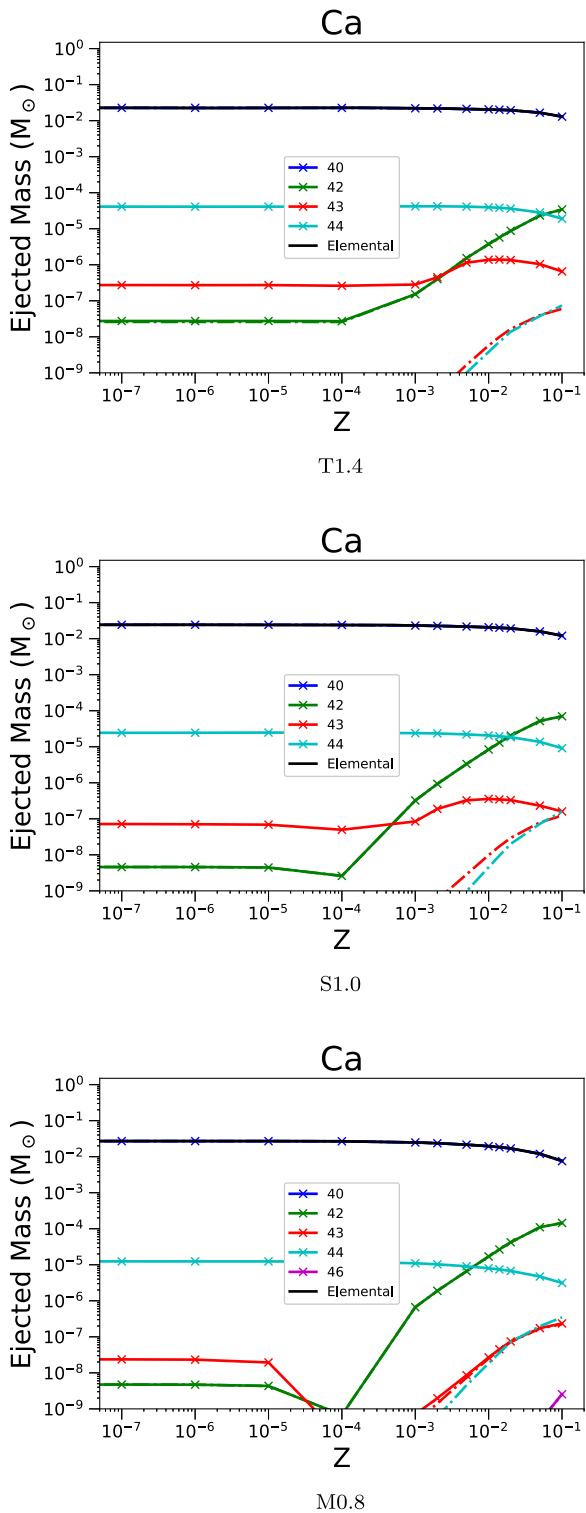
Figure 6. The same as in Figure 4 but for the ejected mass of S, and its stable isotopes ^{32}S, ^{33}S, ^{34}S, and ^{36}S.

Figure 7. As in Figure 4 but for the ejected mass of Ar, and its stable isotopes ^{36}Ar, ^{38}Ar, and ^{40}Ar.

for ^{40}Ca, ^{42}Ca, and ^{44}Ca. The ^{43}Ca trend is similar for T1.4 and S1.0 models. On the other hand, between $Z_{met} = 10^{-4}$ and $Z_{met} = 10^{-2}$, its production drops significantly in the M0.8 models, and it increases again for high metallicities due to its direct production. Only a trace amount of ^{46}Ca is produced in any model, and then only in the M0.8Z0.1 model. ^{48}Ca is not produced in any of our postprocessed models.

The production of ^{40}Ca is fairly simple and consistent throughout the models. A broad production peak is observed in the $Z_{met} = 0$ models in the peak temperature range between 4 and 5.5 GK. As the initial metallicity increases, the yields of ^{40}Ca in this region decrease, resulting in the metallicity trend of ^{40}Ca observed in Figure 8. Between $Z_{met} = 0$ and $Z_{met} = 0.1$, the ejected ^{40}Ca decreases from 2.27×10^{-2} to 1.29×10^{-2}

Figure 8. The same as in Figure 4 but for the ejected mass of Ca, and its stable isotopes ^{40}Ca, ^{42}Ca, ^{43}Ca, and ^{44}Ca.

$M_\odot$ for the T1.4 models, from 2.43×10^{-2} to 1.21×10^{-2} $M_\odot$ in the S1.0 models, and from 2.71×10^{-2} to 7.55×10^{-3} $M_\odot$ in the M0.8 models. The larger effect in the M0.8 model is due to the absence of ejecta at high temperatures.

Not shown here in figures, the production of ^{42}Ca in T1.4Z0 is dominated by a high temperature peak in the 6–7 GK range, with smaller peaks between 4 and 4.3 GK and 8 and 9 GK. The lowest temperature peak is reproduced in the S1.0Z0 and

M0.8Z0 models in the same temperature range. Direct synthesis of ^{42}Ca is the main path for all three classes of model. Production of ^{42}Ca is significantly boosted in the solar and supersolar-metallicity models, where the low-temperature abundance peak observed in the $Z_{met} = 0$ models is increased by several orders of magnitude and covers a peak temperature range from 2–4 GK. This temperature range covers both typical carbon fusion and oxygen fusion conditions, with the largest contribution being in the 3.5–5 GK range. At these temperatures, there is small radiogenic contribution from ^{42}K and ^{42}Ar.

Not shown in the figures presented here, the production of ^{43}Ca in the T1.4Z0 is dominated by the 5.5–7 GK temperature range, where ^{43}Ca is produced as ^{43}Sc with a contribution on the order of 1% from ^{43}Ti. The majority of nucleosynthesis in this temperature range is primary as ^{43}Sc production, and it does not change across metallicities; however, such a radiogenic contribution shows some secondary effects. For the T1.4Z0.014 model, the production below 5 GK shifts to lower peak temperatures, and two components are ejected, peaking at about 2 and 4 GK. In these two regions, ^{43}Ca is produced directly with a small contribution from ^{43}Sc, and with a strong radiogenic contribution from ^{43}K at the coldest peak temperatures.

In the S1.0Z0 model, the maximum peak temperature is approximately 6.2 GK. From around 5.5– 6.2 GK, we see the production of the radioisotope ^{43}Sc; unlike in the T1.4Z0 case, there is no contribution from ^{43}Ti. A region of production in the 4–5 GK range is also present. In the model S1.4Z0.014, this lower-temperature component resolves into a double peaked production region between 2 and 4 GK. Similar to the T1.4 case at analogous metallicity, there is a direct production of ^{43}Ca with a small contribution from ^{43}Sc; however, the carbon region production is boosted in the S1.0Z0.014 model compared with T1.4Z0.014. S1.0Z0.1 also shows a double peak of production between 2 and 4 GK broadening with the radiogenic ^{43}K contribution at lower temperatures. Production is mostly directly as ^{43}Ca, with some contribution from ^{43}K at the lowest peak of production in both the T1.4 and S1.0 cases, and a negligible contribution from ^{43}Sc. Finally, the M0.8 models show the same trends in the 2–5 GK range, as are observed in the T1.4 and S1.0 models.

^{44}Ca is produced primarily as ^{44}Ti in all of the $Z_{met} = 0$ models. In T1.4Z0, it is produced over a wide range of peak temperatures from 4–6.5 GK, with a negligible contribution from a peak at 2.8 GK. We see a similar distribution in the S1.0Z0 and M0.8Z0 models within the temperature range covered in their ejecta as discussed in the previous sections. T1.4Z0.014 shows a small decrease in the production of ^{44}Ti at the lower end of this broad range of production compared to the model at $Z_{met} = 0$. This is partially compensated for by the increased secondary production in the small peak centered at 2.8 GK. Across the rest of the temperature range, we see contributions only from ^{44}Ca and ^{44}Ti, with a small contribution from ^{44}Sc at low peak temperatures. S1.0Z0.014 and M0.8Z0.014 show the same trend. In the $Z_{met} = 0.1$ models, a further suppression of the ^{44}Ti production at the tail end of the broad production range is obtained, with the increase in direct synthesis of ^{44}Ca compensating for this and leading to a continuation of the ^{44}Ca production out to approximately 2.4 GK.

4.5. Titanium

Titanium has five stable isotopes: ^{46}Ti, ^{47}Ti, ^{48}Ti, ^{49}Ti, and ^{50}Ti. Ti isotopes are expected to be produced by both CCSNe and SN Ia. In CCSNe, ^{46}Ti (8.25% of the solar budget) is made by explosive oxygen burning, ^{47}Ti (7.4%) by explosive oxygen burning and explosive silicon burning, ^{48}Ti (73.7%) and ^{49}Ti (5.4%) by explosive silicon burning. ^{50}Ti (5.2%) is mostly produced by the s-process in massive star progenitors (Woosley et al. 2002). While Ti has a significant contribution from SN Ia, its full chemical inventory in the Galaxy is typically not reproduced by GCE simulations when compared to Fe, for instance, making the production of Ti in stars still an open problem for nuclear astrophysics (e.g., Mishenina et al. 2017; Prantzos et al. 2018; Kobayashi et al. 2020a, and references therein).

Figure 9 presents our yields for these isotopes at different metallicities. ^{48}Ti is the most abundant isotope of titanium in all three models for almost all metallicities. Overall, The ejected mass of elemental titanium decreases with increasing progenitor metallicity, driven by the ^{48}Ti nucleosynthesis trend. Only in the M0.8Z0.1 model does ^{46}Ti become more abundant than ^{48}Ti. ^{46}Ti production is primary at $Z < 0.00001$ and secondary above this, with the ejected mass of ^{46}Ti increasing with metallicity. ^{47}Ti has a strong secondary component in the three classes of model above $Z_{met} = 0.001$ through direct production of ^{47}Ti. ^{48}Ti is flat with metallicity in the T1.4 models until $Z > 0.05$, where a strong secondary contribution is seen. For the S1.0 and M0.8 models, this contribution starts at $Z_{met} = 0.001$. The ^{50}Ti yields are high in the T1.4 models and do not depend on the metallicity of the progenitor, with only trace amounts produced in the S1.0 and M0.8 models at $Z > 0.01$. Therefore, the solar ^{50}Ti/^{48}Ti isotopic ratio could be potentially used as a diagnostic to study the relative contribution of different SN Ia progenitors to the solar composition by using GCE simulations.

The ^{46}Ti production at $Z_{met} = 0$ is much more effective in T1.4Z0 than in either of the other two models. This is due to ^{46}Ti being synthesized in intermediate to high explosion temperatures (at 6 GK or above), which do not exist in the S1.0 and M0.8 models. There is a small peak of production at approximately 4 GK, which is negligible. In the $Z_{met} = 0.014$ panels, the production of ^{46}Ti through direct nucleosynthesis is highly dependent on the initial metallicity, with the component at 4 GK now dominating the production. The high-temperature component of the T1.4 models is primary, and does not change with the progenitor composition.

^{47}Ti is produced over a broad range of peak temperatures in the T1.4 models. At $Z_{met} = 0$, production spans the range from explosive oxygen fusion through to NSE, from around 4–9 GK, with peaks between 5.5 and 7 GK contributing to the majority of the ejecta. Across the whole temperature range, ^{47}Ti is mostly ejected as ^{47}V, with a minor direct production between 8 and 9 GK and a negligible ^{47}Sc production at around 9 GK. For the T1.4Z0.014 model, a direct ^{47}Ti production peak is formed between 2.3 and 4.2 GK. In the ejecta of T1.4Z0.1, the ^{47}Ti yields have increased further in the lower peak temperature regions, with ^{47}Ti now accounting for a significant fraction of the ejected Ti mass. Also in the S1.0 and M0.8 models, the radiogenic ^{47}V contribution is important for the ^{47}Ti yields, which are strongly metallicity dependent. In model S1.0Z0, the bulk of production is between 3.8 and 6.1 GK. In models S1.0Z0.014 and M0.8Z0.014, the direct ^{47}Ti production

becomes relevant at low peak temperatures, and it then dominates the isotope yields at $Z_{met} = 0.1$.

In the T1.4 set, ^{48}Ti is made over a broad range of peak temperatures, ranging from about 4 GK to the high-density NSE region at temperatures larger than 9 GK. Above 8.2 GK, ^{48}Ti is made directly. Below 8.2 GK, ^{48}Ti is mostly produced as ^{48}Cr, with a negligible contribution from ^{48}V. In T1.4Z0.014 and T1.4Z0.1, the isotope yields extend into the temperature range between 2.3 and 3.8 GK. Here, ^{48}Ti is produced directly, and it is metallicity dependent. In the S1.0Z0 model, the ^{48}Ti in the 3.5–6.1 GK temperature region is solely produced as ^{48}Cr. Similar to the T1.4 and the M0.8 model sets, we obtain a direct production of ^{48}Ti in the 2.8–3.8 GK range in the high-metallicity models.

^{49}Ti production in T1.4Z0 ranges from 3.8 GK to > 9GK, with three peaks of production between 3.8 and 6 GK, 7 and 8 GK, and above 9 GK, respectively. The majority of ^{49}Ti is produced as ^{49}Cr, particularly below 8 GK, where almost 100% of the ejecta is radiogenic ^{49}Cr. Only trace amounts of radiogenic ^{49}Mn and ^{49}V are present. Between 8 and 9 GK, there is a small region where production is dominated by contributions from radiogenic ^{49}V, and above 9 GK we obtain a direct production of ^{49}Ti. These two components, however, are small compared to the ^{49}Cr yields. In the T1.4Z0.014 model, we see a significant increase in the 4–6 GK temperature region. Peak production in these particles increases by an order of magnitude between these two models. We also see an increase in the contribution from ^{49}V, between 2.3 and 3.5 GK. In the T1.4Z0.1 model, this low-temperature contribution is depleted, due to increased neutron captures shifting material to more neutron-rich isotopes. We also see a further increase in the 4.5–6 GK region, which drives the increasing ejected mass of ^{49}Ti with initial metallicity. The models of the S1.0 and M0.8 sets show a similar behavior for the two lower-temperature components shared with the T1.4 models.

Regarding ^{50}Ti, in T1.4Z0 the only relevant contribution is from the particles with peak temperature $T > 8$ GK. As such, neither the S1.0 nor M0.8 model produce ^{50}Ti at $Z_{met} = 0$. As the metallicity increases, we see a small production of ^{50}Ti between 3 and 3.5 GK for all models. This is reproduced in S1.0Z0.014 and M0.8Z0.014, where production is slightly larger than in the T1.4 model. In all cases, however, the ^{50}Ti yields at lower peak temperatures remain small.

4.6. Vanadium

We see in Figure 10 that vanadium has a similar trend with metallicity through our three model sets. There is, however, around a factor of 10 difference between the total yields of the T1.4 models compared to the M0.8 yields. We also observe a dip in production for the M0.8 models at $Z_{met} = 10^{-4}$, which is not present in the other models. Trace amounts of ^{50}V (0.25% of the solar budget of V) are produced at all metallicities in the T1.4 models, with a weak secondary component, whereas in the S1.0 and M0.8 models, we obtain the same secondary component but without any primary ejecta.
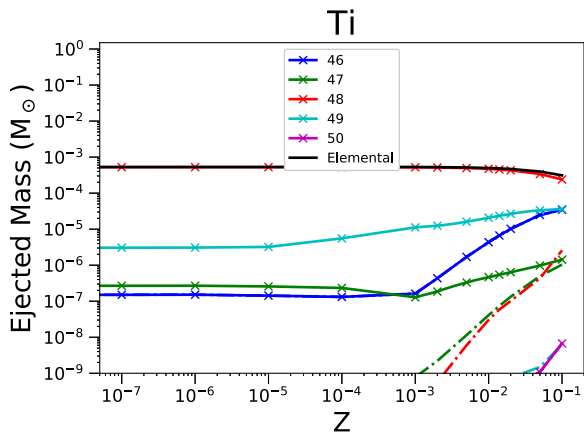
The primary ^{50}V component (99.75% of the solar budget) in the T1.4 models is ejected with the hottest particles, with a maximum temperature peak > 8 GK. This is obviously not present in the other sets with smaller SN Ia progenitors. The secondary ^{50}V component arises in the 2.5–4 GK temperature range, at solar and supersolar metallicity.
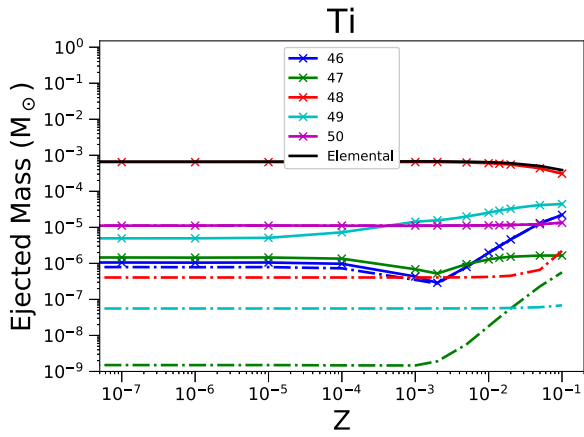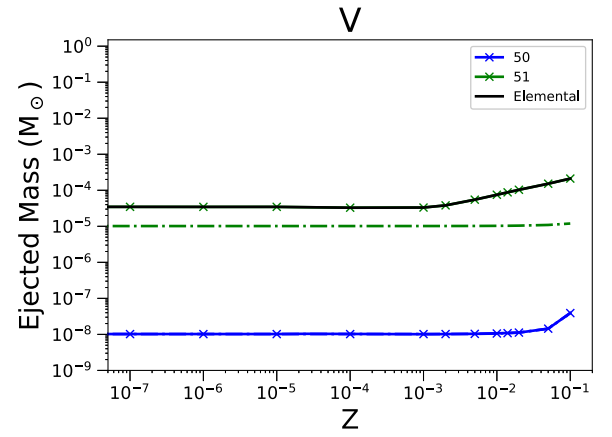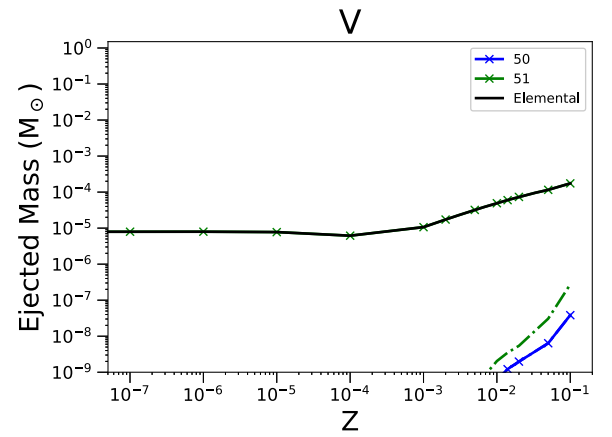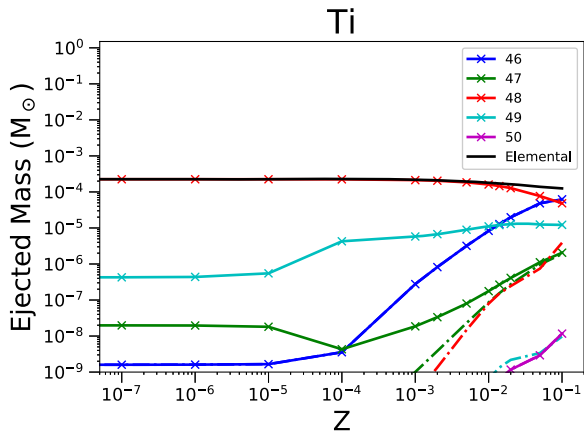
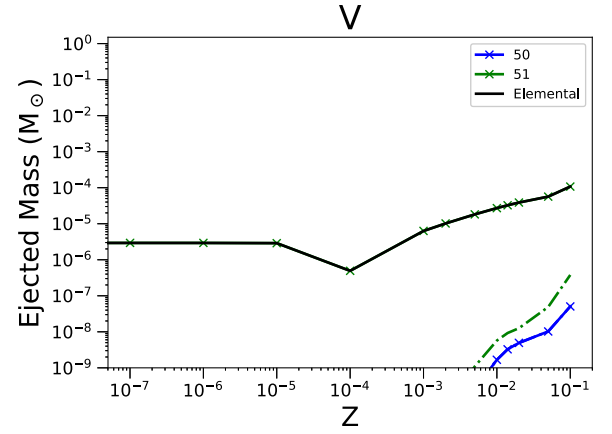**Figure 9.** As in Figure 4 but for ejected mass of Ti, and its stable isotopes ^{46}Ti, ^{47}Ti, ^{48}Ti, ^{49}Ti, and ^{50}Ti.

Figure 10. The same as in Figure 4 but for the ejected mass of V, and its stable isotopes ^{50}V and ^{51}V.

Production of ^{51}V is significantly more complex than ^{50}V, particularly in the T1.4 models. In model T1.4Z0, the highest peak temperature particles above 9 GK directly produce ^{51}V. At lower peak temperatures, from approximately 7.8–8.5 GK, ^{51}Cr becomes the largest contributor. Finally, for temperatures < 7.8 GK, the synthesis of ^{51}V is mostly dominated by radiogenic ^{51}Mn. We also see a trace contribution from ^{51}Fe in this model, but it is small in comparison to the other

contributing isotopes. For model T1.4Z0.014 and T1.4Z0.1, the high-temperature contribution to the isotopic abundance of ^{51}V remains the same. The low-temperature contribution from ^{51}Cr increases, causing an increase in the ^{51}V yields. The synthesis of ^{51}Mn is the main route for production in model S1.0Z0, with a trace contribution from radioactive ^{51}Cr. This production occurs over a broad range of temperatures, but is much less abundant than in the T1.4 cases. In models

S1.0Z0.014, the production of ^{51}Cr at lower temperatures begins to contribute significantly to the overall ejected mass of ^{51}V. This trend increases as we move to model S1.Z0.1, where the contributions from ^{51}Mn and ^{51}Cr become comparable. The contribution from ^{51}Mn occurs above peak temperatures greater than 4.5 GK and ^{51}Cr below this. Production in the M0.8 models follows a similar trend to the S1.0 models. M0.8Z0.1 shows a much larger ^{51}Cr to ^{51}Mn production due to the smaller number of particles at higher peak temperatures, and the lower maximum peak temperature in this model.

4.7. Chromium

Chromium has four stable isotopes: ^{50}Cr, which has a half-life of 1.3×10^{18} yr, and we therefore treat as stable, as well as ^{52}Cr, ^{53}Cr, and ^{54}Cr. ^{52}Cr is the most abundant Cr isotope in the Sun (83.789 % of the solar Cr), while ^{54}Cr has the lowest abundance (2.365 % of the solar Cr; Lodders 2003; Asplund et al. 2009).

SN Ia are major contributors to the solar Cr budget (Kobayashi et al. 2020a). In Figure 11, we show the integrated Cr yields for the element and its isotopes, for the T1.4, S1.0, and M0.8 sets. Cr production is dominated by ^{52}Cr for all metallicities in the T1.4 and S1.0 sets. At metallicities higher than solar, in the M0.8Z0.1 models, ^{50}Cr and ^{53}Cr production increases enough as the metallicity of the progenitor increases to affect the Cr abundance, causing an increase of its total ejected mass. Except for this pattern at high metallicities, Cr production appears to be primary in all models following the ^{52}Cr trend. On the other hand, the relative production of different Cr isotopes changes significantly with metallicity and using different model sets. ^{50}Cr is the only isotope that is always produced directly. ^{54}Cr is mostly ejected as itself in T1.4 models, while for other sets it is mostly radiogenic. ^{52}Cr and ^{53}Cr are produced by radiogenic contribution in all of the explosion models. For all sets, the yield of ^{50}Cr rises with increasing metallicity of the WD progenitor above a threshold value of $Z_{met} = 10^{-4}$. ^{53}Cr shows a much weaker rise, and ^{54}Cr is mostly primary for T1.4 models, while its (much weaker) production is secondary for other sets.

In the T1.4 set, the ^{50}Cr yields are dominated by two production peaks, at 7–9 GK and 3–5 GK temperature, respectively. The first peak is primary, while the low-temperature peak is secondary, rising with increasing metallicity. Only the T1.4Z0 model shows a relevant radiogenic contribution by ^{50}Mn at lower temperatures, but the production is dominated by the first peak. S1.0 and M0.8 sets only carry the secondary peak, explaining their smaller ^{50}Cr production at low metallicities compared to T1.4. On the other hand, for all sets, the strong secondary component in ^{50}Cr causes this isotope to form up to about 10% of all Cr ejecta (M0.8Z0.1 model). The ^{52}Cr abundance pattern is significantly more complex than ^{50}Cr, revealing a larger number of production channels. For the T1.4 set, primary ^{52}Cr is directly produced in the hottest ejecta, with temperatures above 8 GK. Two additional peaks, from the eventual decay of ^{52}Fe, occur at around 7 GK and 5 GK. These are insensitive to the initial metallicity of the model, and contribute the majority of ^{52}Cr. Finally, we obtain a secondary production of ^{52}Cr at about 4 GK in the T1.4Z0.014 and T1.4Z0.1 models. Small amounts of ^{52}Mn are also produced in all models. The S1.0 and M0.8 models all show the primary ^{52}Fe production, and the secondary ^{52}Cr channel at lower temperatures. The ^{53}Cr

isotope is produced directly above 9 GK in the innermost ejecta for the T1.4 set. For 8–9 GK, the production is dominated by a primary peak of radiogenic ^{53}Mn. Two additional ^{53}Mn channels appear at lower temperatures, with the colder production peak in oxygen burning conditions becoming particularly relevant at supersolar metallicities. Two broad primary peaks at 7–8 GK and about 5 GK are due to the radiogenic contribution from ^{53}Fe. ^{53}Fe continues to be the primary radiogenic source of ^{53}Cr in the S1.0 and M0.8 sets. In agreement with T1.4 models, a secondary production of ^{53}Mn and ^{53}Cr is obtained at 3–4 GK. Finally, ^{54}Cr is produced directly at temperatures above 8 GK, while a secondary production peak is present at about 4 GK from the radiogenic decay of ^{54}Mn.

4.8. Manganese

Mn is monoisotopic, with only ^{55}Mn being stable. In CCSNe, it is mainly formed in explosive silicon burning, with some possible contribution from the neutrino-winds component (Woosley et al. 2002). The production of Mn with respect to Fe in SN Ia has been the subject of a number of GCE investigations (Kobayashi et al. 2006; Seitenzahl et al. 2013a; Kobayashi et al. 2020a; Eitner et al. 2020), as both Mn and Fe in the Milky Way disk and in the Sun are produced primarily by SN Ia (Matteucci et al. 2009; De los Reyes et al. 2020). Mn has also been proposed as a key tracer for differentiating the relative contribution from SN Ia progenitors of different masses (e.g., Seitenzahl et al. 2013a; Eitner et al. 2020). Kobayashi et al. (2020b) identified a positive correlation for the production of Mn with respect to initial metallicity, similar to the results presented here. They, however, saw a decrease in the ejected mass of Mn with increasing progenitor mass, at odds with the findings of Seitenzahl et al. (2013b) and this work. Finally, based on GCE simulations, SN Iax were discussed as a possible important source to the galactic Mn abundance (Cescutti & Kobayashi 2017; Kobayashi et al. 2020b), although this is still a matter of debate (Eitner et al. 2022). SN Iax are a subclass of SN Ia, which are spectroscopically similar to SN Ia explosions but with lower ejecta velocities and lower peak magnitudes, as described in Foley et al. (2013). Figure 12 shows the ejected mass of Mn from our three models with respect to metallicity, indicating a large radiogenic contribution across the range of Z investigated. This result is expected and consistent with previous results in the literature. For instance, Truran et al. (1967) already identified Mn as being mainly produced as ^{55}Co.
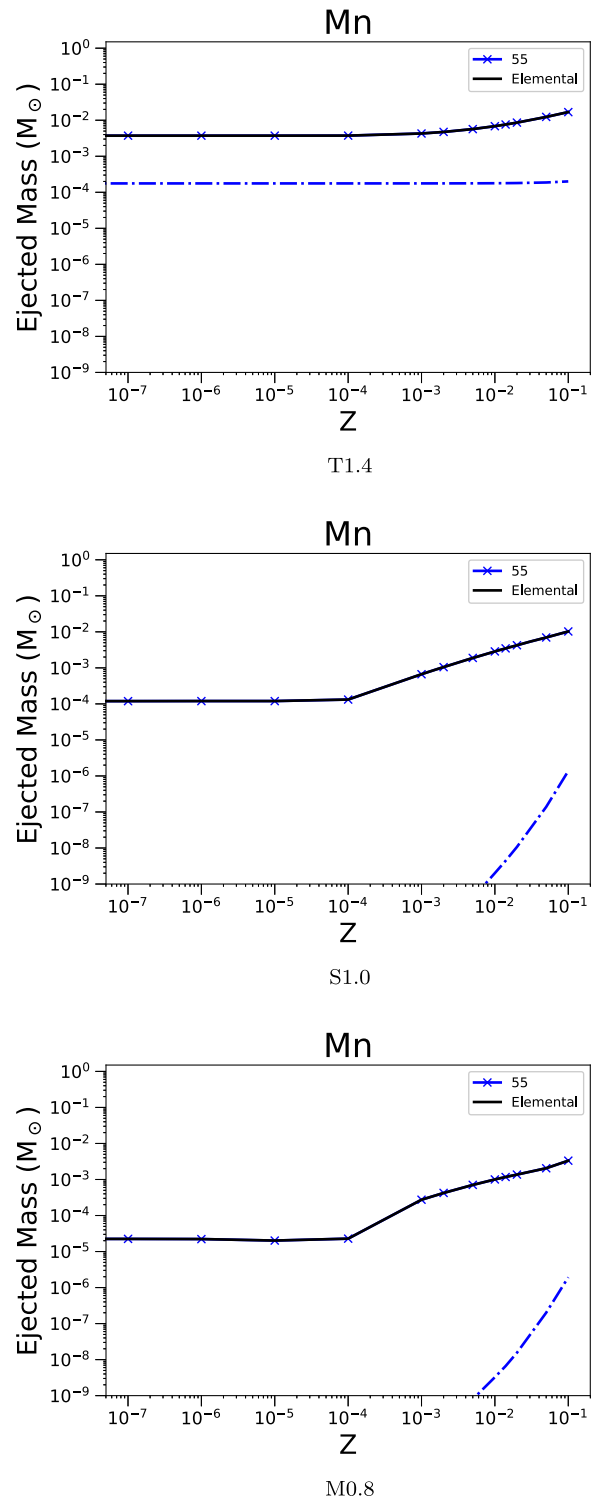
In the low-metallicity sub-Chandrasekhar-mass models, most production of Mn is as ^{55}Co, with a negligible contribution from ^{55}Fe. This contribution increases with increasing initial metallicity as the secondary ^{55}Fe component begins to dominate at lower temperatures (between 3 and 4 GK). The production of ^{55}Co is also boosted by this secondary component in both the S1.0 and M0.8 models, increasing the overall production of ^{55}Mn. In the T1.4 models, we see that the production of ^{55}Fe is again boosted at higher metallicities, with a small peak of ^{55}Mn contributing at lower temperatures in these models, although this peak has a negligible impact on the total production of Mn. We see that the trace amount of ^{55}Ni produced at intermediate temperatures in this model is suppressed with increasing initial ^{22}Ne abundance while ^{55}Fe production is boosted throughout the model. ^{55}Cr production is comparable to the radiogenic ^{55}Fe contribution, in contrast with
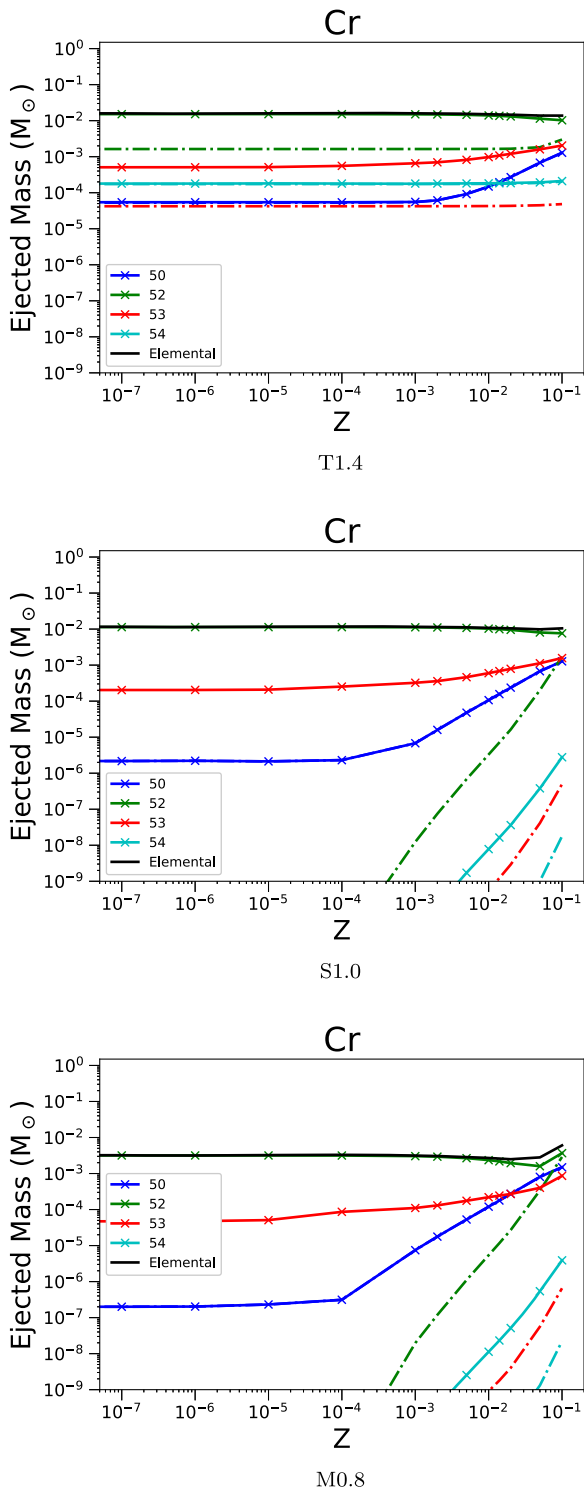
Figure 11. The same as in Figure 4 but for the ejected mass of Cr, and its stable isotopes ^{50}Cr, ^{52}Cr, ^{53}Cr, and ^{54}Cr.

Figure 12. The same as in Figure 4 but for the ejected mass of ^{55}Mn.

the lower-mass models where it is the dominant radiogenic contribution.

Seitenzahl et al. (2013a) also found that ^{55}Co is the largest contributor to manganese yields at densities above 2×10^8 g cm^{-3}. In the T1.4 models, these densities cover the full range of peak temperatures (although not all of the particles have a density above this threshold density). In particular, ^{55}Co is the dominant source of ^{55}Mn in the T1.4Z0 model, and remains the

largest contributor to ejected ^{55}Mn mass. The relative contribution from ^{55}Fe in the T1.4 models increases with increasing metallicity and at $Z_{met} = 0.1$ contributes on the order of 10% of the ejected ^{55}Mn mass. Finally, there is also a contribution from direct synthesis of ^{55}Mn in the highest-temperature regions; however, this is small—of the order of 1% of total ejected mass of ^{55}Mn in the T1.4Z0 model. Eitner et al. (2020) considered the fraction of sub-Chandrasekhar-mass SN

Ia to be as high as 75%, due to the large [Mn/Fe] ratios possible in these low-mass models.

4.9. Iron

Iron has four stable isotopes: ^{54}Fe (5.8% of the solar budget), ^{56}Fe (91.75%), ^{57}Fe (2.1%), and ^{58}Fe (0.3%). In CCSNe, ^{54,56,57}Fe are all produced in explosive silicon burning, and ^{58}Fe is produced efficiently by the s-process during the evolution of the stellar progenitor (Woosley et al. 2002). Around 70% of the solar Fe is produced, however, by SN Ia explosions (Matteucci & Greggio 1986).

In Figure 13, the ejected mass of the stable Fe isotopes is given, along with their radiogenic contributions, as a function of initial metallicity. There is a small decrease in the abundance of elemental Fe ejected from the T1.4 and S1.0 models due to a reduction in the ejected mass of ^{56}Fe with increasing initial metallicity. This is partially compensated for by an increase in the abundances of ^{54}Fe in these two models, which occurs sharply at $Z_{met} = 0.0001$ in the S1.0 and M0.8 models, and more gradually at supersolar metallicities in the T1.4 model. The increase of over 2 orders of magnitude in the abundance of ^{54}Fe becomes a significant contributor to the overall abundance of Fe in T1.4 models at supersolar metallicities. ^{54}Fe is produced directly in all models.

^{56}Fe is one of the largest components of the ejecta of all of the models. While M0.8 has a smaller contribution than the others, most metallicities still have mass fractions of ^{56}Fe above 10%. In T1.4, the production is dominated by the ^{56}Ni yields, with a nonnegligible contribution from the direct synthesis of ^{56}Fe at higher metallicities. This is offset by the reduced ^{56}Ni production at intermediate peak temperatures from the $Z_{met} = 0.014$ and $Z_{met} = 0.1$ metallicity models. Notice also that ^{56}Fe is produced directly at temperatures above 8 GK, the component of which is insensitive to metallicity effects. A more pronounced effect on the overall abundance of ^{56}Fe with metallicity is obtained in the $0.8 M_\odot$ model. However, the iron production actually increases for M0.8 at higher metallicities, due to a significant contribution from ^{54}Fe. ^{57}Fe has a large radiogenic contribution across all models. The ^{57}Fe amount produced directly by the explosion accounts for 1% of the total mass of the ^{57}Fe yields in the T1.4 models, and it is negligible in the S1.0 and M0.8 sets, where almost all production is through radiogenic contributions. The radioactive isotopes ^{57}Ni and ^{57}Co are the main contributors to the ^{57}Fe yields, particularly in the lower-mass models. There is a small contribution to ^{57}Fe abundance from ^{57}Mn and ^{57}Cu in T1.4, but it is negligible. Primary production of ^{57}Fe occurs in models at higher metallicity, in low explosion temperature peaks. This constitutes a small fraction of the total ejected mass of ^{57}Fe. ^{57}Co production is boosted at higher metallicities, driving the increasing trend in all models in Figure 13. Finally, not shown in the figures, we have ^{58}Fe, where only trace abundances are produced in the sub-Chandrasekhar models. Its production in T1.4 models is consistent over a range of metallicities with an ejected mass of the order of 0.001 $M_\odot$. At lower temperatures, ^{58}Fe nucleosynthesis is very similar between our three sets of models as the initial metallicity increases, with radiogenic ^{58}Co contributing to most of ^{58}Fe ejecta. At the highest temperature peaks in the T1.4 models (greater than 8.5 GK), most of ^{58}Fe is produced directly.

Timmes et al. (2003) investigated the impact of the initial metallicity of the stellar progenitor on the Fe production in SN Ia, and found that by varying the metallicity from 0.1–10 times the solar value, the Fe production decreases by 25%. In this work, models T1.4 and S1.0 show similar Ni trends with metallicity (Figure 14), which is the main component of ejected Fe and is in agreement with the results of Timmes et al. (2003). The M0.8 model, however, does not show the same linear dependence as the higher-mass models. We instead see a much sharper decrease in the ejected ^{56}Ni mass, down to around 30% of the initial ejected mass at $Z_{met} = 0$.

4.10. Cobalt

^{59}Co is the only stable isotope of cobalt. In CCSNe, it can be produced in a variety of stellar conditions—by the s-process, the α-rich freeze-out, and by neutrino-winds (Woosley et al. 2002). Additionally, Kobayashi et al. (2020a) highlighted that Co also has a small contribution from SN Ia events. In all of the SN Ia models shown in Figure 15, ^{59}Co has significant contributions from radiogenic sources. We see that for the cases of S1.0 and M0.8, there is a strong secondary effect in both the direct and radiogenic synthesis of ^{59}Co, starting at $Z_{met} = 0.001$. In T1.4, there is no strong dependency on metallicity. The production of cobalt shows an increasing efficiency with an increase in the mass of the SN Ia progenitor. M0.8 models show the strongest metallicity dependence, with an increase in production of almost 3 orders of magnitude between the model at $Z_{met} = 0.001$ and the maximum at $Z_{met} = 0.1$.

The radiogenic contribution to ^{59}Co is dominated by ^{59}Ni at peak temperatures between 7.5 and 8.5 GK and ^{59}Cu at intermediate and lower peak temperatures. ^{59}Co is produced directly only for $T > 8.5$ GK. The radiogenic production of cobalt is insensitive to metallicity effects at temperatures above 5 GK. The ^{59}Ni ejecta is uniform across T1.4 models at temperatures exceeding 7 GK, and the increase at around $T = 4$ GK in models T1.40.014 and T1.4Z0.1 is small compared to contributions from deeper layers. In the intermediate peak temperature range, ^{59}Cu nucleosynthesis is broadly insensitive to varying metallicity. Since this component contributes a majority of the ^{59}Co production in this model, the Co production will be mostly primary. The small ^{59}Zn production found in model T1.4Z0 is suppressed at metallicities above $Z_{met} = 0$. The ^{59}Co yields in the S1.0 models are dominated by two components: a large, narrow peak for $T > 5.5$ GK, and a broader shallower peak between 3.5 and 5.5 GK. In the S1.0Z0 model, both of these Co peaks are dominated by radiogenic ^{59}Cu. As initial metallicity rises, the production of ^{59}Cu is suppressed in the lower-temperature peak, and the secondary component of ^{59}Ni is boosted. In model S1.0Z0.1, production of ^{59}Ni is boosted to the extent that it is comparable with the total contribution of ^{59}Cu. In the M0.8 models, the amount of ^{59}Co ejected is severely reduced as compared with the previous sets of models. M0.8Z0 has a small peak between 3.2 and 5 GK, where the main contributor to the ejected cobalt mass is from radioactive ^{59}Cu. As seen in the S1.0 models, production of ^{59}Cu is suppressed at higher metallicities, where the radioactive isotope ^{59}Ni provides a crucial contribution to the final Co yields.

4.11. Nickel

Nickel is composed of five stable isotopes: ^{58}Ni (68% of the solar budget), ^{60}Ni (26%), ^{61}Ni (1.1%), ^{62}Ni (3.6%), and ^{64}Ni (0.9%). In CCSNe, the isotopes ^{58,60,61,62}Ni are produced
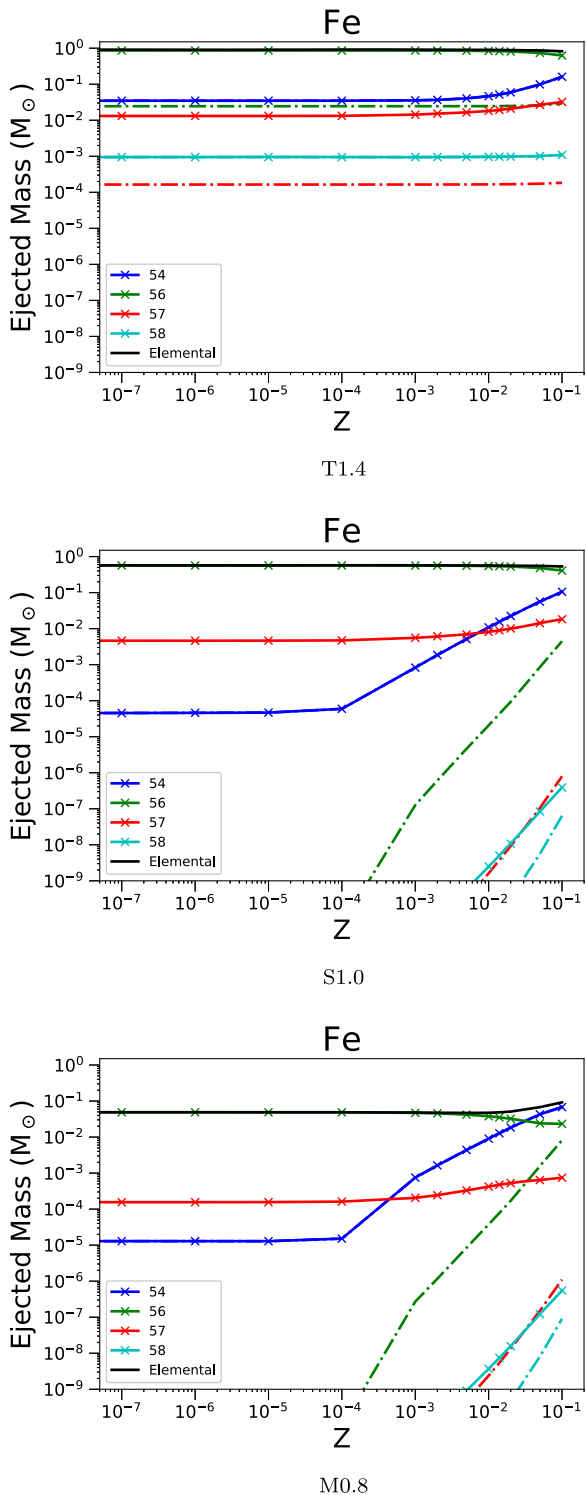
Figure 13. The same as in Figure 4 but for the ejected mass of Fe, and its stable isotopes ^{54}Fe, ^{56}Fe, ^{57}Fe, and ^{58}Fe.

during the α-rich freeze-out from NSE (Woosley et al. 2002), while the s-process makes the majority of the solar ^{62}Ni and ^{64}Ni and possibly a significant fraction of ^{60}Ni and ^{61}Ni (e.g., Pignatari et al. 2016). According to GCE simulations, however, most of the solar Ni is made by SN Ia (Kobayashi et al. 2020a, and references therein).

Figure 16 shows the Ni abundance trend with metallicity with the highlighted radiogenic contributions. In the T1.4

models, there is an increase in the ejected mass of nickel at around $Z_\odot$, moving from about $5 \times 10^{-2} M_\odot$ to over 0.1 $M_\odot$ at $Z_{met} = 0.1$, driven by an increase in the production of ^{58}Ni. In S1.0, we see a similar increase from a lower initial yields of approximately $6 \times 10^{-3} M_\odot$ to nearly 0.1 $M_\odot$. In the M0.8 set, the abundance of ^{58}Ni increases from a low $2.5 \times 10^{-5} M_\odot$ at $Z_{met} = 0$ to $3.6 \times 10^{-3} M_\odot$ at $Z_{met} = 0.1$.

In all models, ^{58}Ni is mostly produced directly with only a small radiogenic contribution. In the T1.4 models, the ^{58}Ni isotope production in the hottest central ejecta is largely insensitive to the initial composition, although the minor radiogenic contributions from ^{58}Cu decrease in the 5–6 GK explosion temperature range. The models S1.0 and M0.8 do not include such a high-temperature component. As a consequence, their total ^{58}Ni yields are much smaller, but also more affected by the initial metallicity, increasing the ejected ^{58}Ni mass by over an order of magnitude over the metallicity range investigated.

The metallicity dependence of ^{60}Ni yields is similar for models T1.4 and S1.0, where the ejected mass of ^{60}Ni decreases with increasing metallicity above approximately $Z_{met} = 10^{-2}$ (T1.4 set) and $Z_{met} = 2 \times 10^{-3}$ (S1.0 set; Figure 16). In T1.4Z0, we obtain three areas of production: one above 8 GK, one between 5 and 7 GK, and a smaller peak between 4 and 5 GK. In the 8–9 GK region, ^{60}Ni is directly produced, while in the 5–6 GK peak, most ^{60}Ni is synthesized as ^{60}Zn. This contribution decreases with increasing metallicity, driving the shallow decline of ejected ^{60}Ni. In the T1.4Z0.014 model, the low-temperature peak has been boosted significantly with direct production of ^{60}Ni. The ^{60}Ni production also extends further down to lower explosion temperatures around 3.5 GK. This trend continues in T1.4Z0.1, where there is a significant boost to the ^{60}Ni production in the intermediate-temperature region. In model S1.0, the highest temperature peak is missing, as no particles experience these conditions. We therefore obtain a much stronger metallicity dependence on the ^{60}Ni for this model, with the total ejected mass of ^{60}Ni decreasing as the metallicity increases. This is due to the same effects driving the decrease in the T1.4 models, namely, a drop in the production of ^{60}Zn in the intermediate peak temperature region. However, as there is not a large contribution from $T > 6$ GK regions in the S1.0 models, there is proportionally a much larger effect. In the M0.8 models, we obtain even smaller ^{60}Ni yields. Similar to S1.0Z0, the analogous M0.8 model shows the ^{60}Ni yields mostly made by radiogenic ^{60}Zn. At higher metallicity, there are no relevant contributions from radioactive isotopes.

In the T1.4 model sets, the ^{61}Ni production is dominated by the intermediate- and high-temperature regions. The ejected mass of ^{61}Ni is mostly primary, and changes from $2.06 \times 10^{-4} M_\odot$ at $Z_{met} = 0$ to $3.89 \times 10^{-4} M_\odot$ at $Z_{met} = 0.1$. In the high-temperature region, ^{61}Ni is directly produced, and in the intermediate peak temperature region, ^{61}Zn is the major contributor to ejected ^{61}Ni mass. Finally, in the low-temperature region, ^{61}Ni is produced directly. For the S1.0 models, ^{61}Ni is also primary. Production in the intermediate peak temperature region is insensitive to an increase in the initial ^{22}Ne mass fraction, with ^{61}Ni being synthesized as ^{61}Zn, as in the T.14 models. The low-temperature region is directly produced as ^{61}Ni, and contributes only of the order of 0.1%–1% of the ejected mass of ^{61}Ni in this model. With the high-temperature region missing, the total ejected mass of ^{61}Ni compared with the T1.4 models is a factor of 2 lower. In the
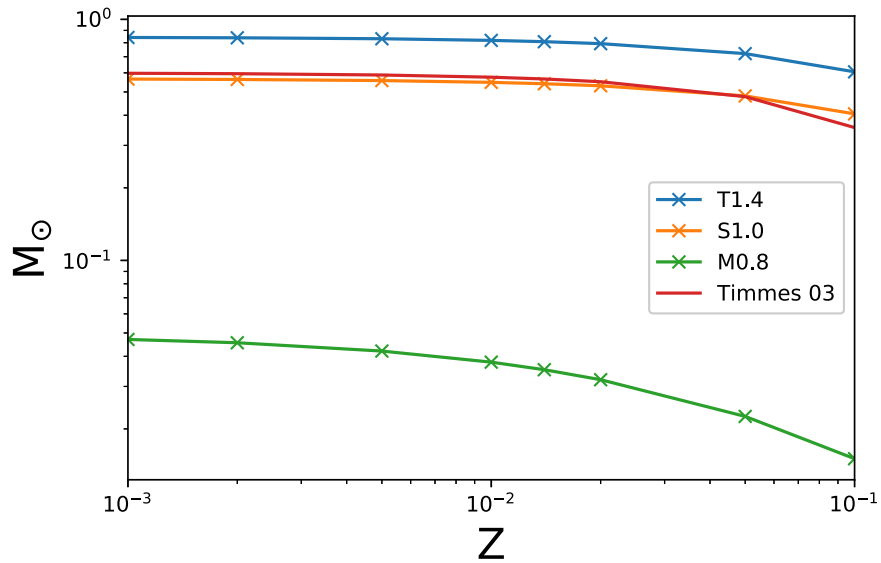
Figure 14. Ejected mass of ^{56}Ni as a function of initial metallicity for our models, compared with Timmes et al. ([2003](#)) calculations.

M0.8 models, both the intermediate- and high-temperature peaks are missing, and so we only obtain a small contribution at explosive temperature peaks of about 4 GK.

Not shown in the figures, the nucleosynthesis of ^{62}Ni is very similar to that for ^{61}Ni, with a large contribution from the high- and intermediate-peak-temperature regions. In the T1.4 models, we see that the direct production of ^{62}Ni in the 8–9 GK temperature range is larger than the production of ^{61}Ni in that same region. The intermediate peak temperature region from around 5–7 GK is very similar to the ^{61}Ni production region in the T1.4 models, with the mass fraction of ^{62}Ni being around 0.1%. ^{62}Zn is the major contributor to abundances in this region, as the direct production drops for temperature peaks lower than 8 GK. The production in this region is sensitive to the initial metallicity, increasing from the initial approximately 0.2% by mass fraction in T1.4Z0 to around 3% in model T1.4Z0.1. We also see a small contribution at lower temperatures through direct production of ^{62}Ni, although this has a negligible effect on the ejected mass. In the S1.0 series of models, we again find an increase in the production at intermediate peak temperatures with the initial metallicity. As the highest temperatures in this model are at approximately 6 GK, we see only the lower end of the production region at high temperatures, which significantly reduces the ejected mass of ^{62}Ni. In the models M0.8, there is no production at $Z_{met} = 0$, and only a marginal production at $Z_{met} = Z_\odot$. The 6 GK region is completely absent from this model, and so the production through the formation of ^{62}Zn is not possible. Finally, the ^{64}Ni production is confined to the high peak temperature region above 8 GK, which is only found in the T1.4 models.

4.12. Zinc

Zinc has five stable isotopes: ^{64}Zn (49.2% of the solar budget), ^{66}Zn (27.7%), ^{67}Zn (4%), ^{68}Zn (18.5%), and ^{70}Zn (0.6%). None of the models investigated here produce ^{70}Zn; as such, we will not discuss this isotope further. In CCSNe, ^{64}Zn is mostly produced by neutrino driven winds, in α-rich freeze-out conditions, and a small s-process contribution is also possible (Woosley et al. [2002](#)). ^{66}Zn is efficiently produced by the s-process and the α-rich freeze-out, and ^{68}Zn is produced

mostly in massive stars through the s-process (Woosley et al. [2002](#)). Nevertheless, Kobayashi et al. ([2020a](#)) showed that Zn also has a small contribution from SN Ia.

Zinc production in the models T1.4 and S1.0 is similar (Figure [17](#)). Zn yields decrease at around $Z_{met} = 0.001$ by approximately a factor of 5, following the trend of ^{64}Zn. At the same time, ^{66}Zn production increases, becoming the most abundant isotope at higher metallicities.

Not shown in the figures, in all T1.4 models the ^{64}Zn nucleosynthesis is dominated by the radioactive isotope ^{64}Ge. The contribution of ^{64}Ga to the ejected abundance increases at higher metallicities as the intermediate peak temperature range production of ^{64}Ge shrinks. In the S1.0 models, the ^{64}Zn production is also primarily through synthesis of ^{64}Ge. The decrease in the overall production of ^{64}Zn follows the reduction in ^{64}Ge and ^{64}Ga produced at peak temperatures around 5.5–6 GK. We also observe the rise in direct production of ^{64}Zn with increasing metallicity, although the absolute abundance is only of the order of 5% in the S1.0Z0.1 model. The production of ^{66}Zn is largely centered in the intermediate peak temperature range starting at approximately 5.2 GK and continuing to 8 GK. ^{66}Zn is mostly produced as ^{66}Ge in the T1.4Z0 model, with trace amounts of other isotopes. Production is nearly identical in the T1.4Z0.014 model, with only a slight increase in the production of ^{66}Ga (but still only a negligible contribution). Production in all three S1.0 models is similar, with a strong radiogenic contribution to ^{66}Ge. Trace amounts of ^{66}Ga do not affect the overall yields.

^{67}Zn has a similar trend as for ^{66}Zn. In model T1.4Z0, there is a comparable contribution to the ejected mass of ^{67}Zn from both ^{67}Ge and ^{67}As. As the initial metallicity increases, both of these contributions become small compared to the increased production of ^{67}Zn, culminating in T1.4Z0.1, where only trace amounts of ^{67}Ge and ^{67}Cu contribute to the abundance of ^{67}Zn.

The production of ^{68}Zn occurs mainly at intermediate peak temperatures from 5.2–7 GK. In the model T1.4Z0, there is a small contribution to ^{68}Zn from ^{68}As, with the bulk of material being synthesized as ^{68}Se. ^{68}Se production is reduced as the metallicity increases, leading to an overall decrease in the ejected mass of ^{68}Zn and increase in the ^{68}Ge to ^{68}Se ratio. In model T1.4Z0.1, ^{68}Se is no longer the most abundant isotope,
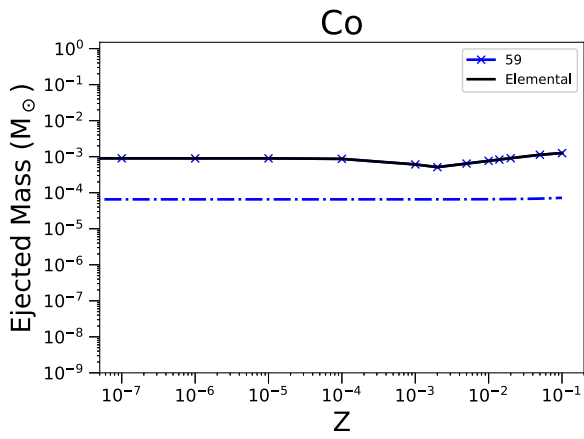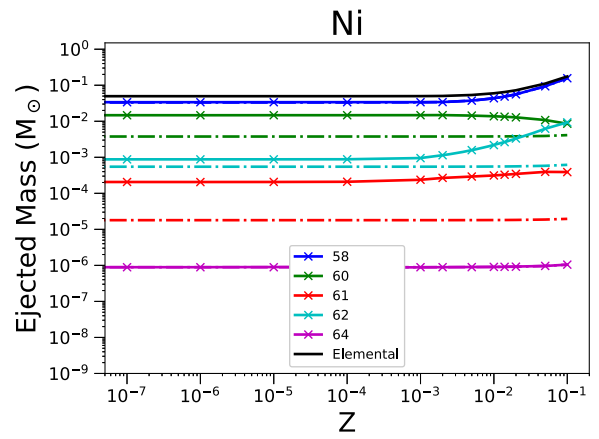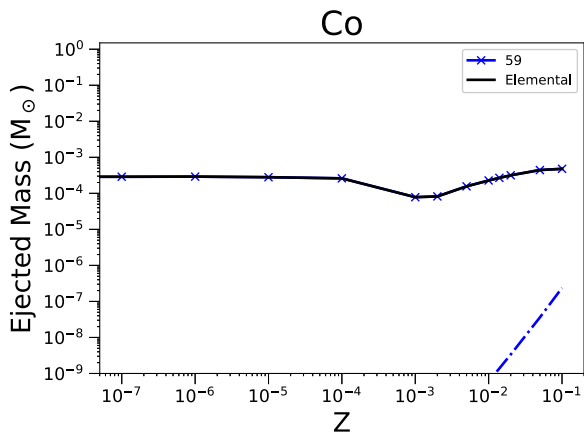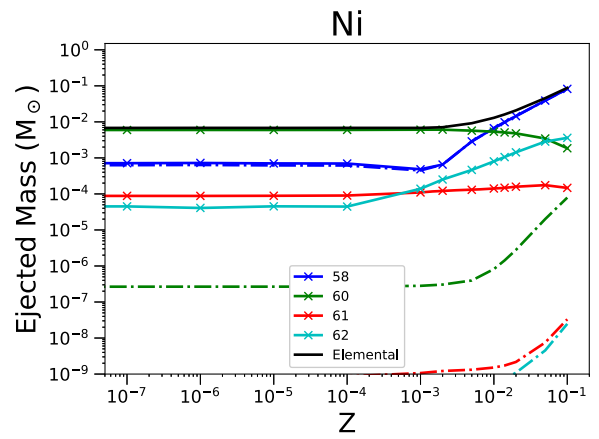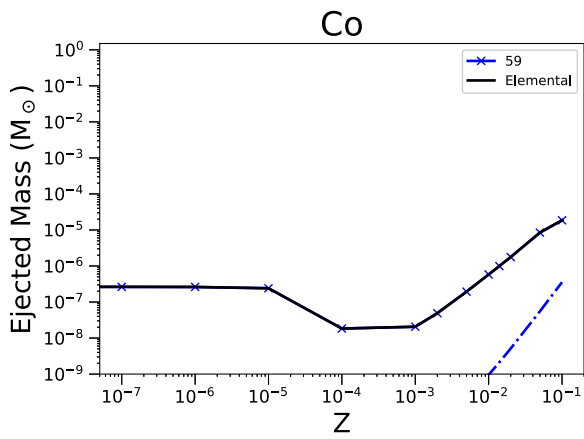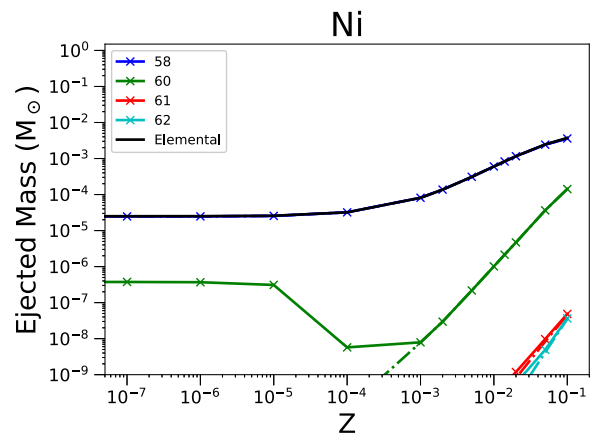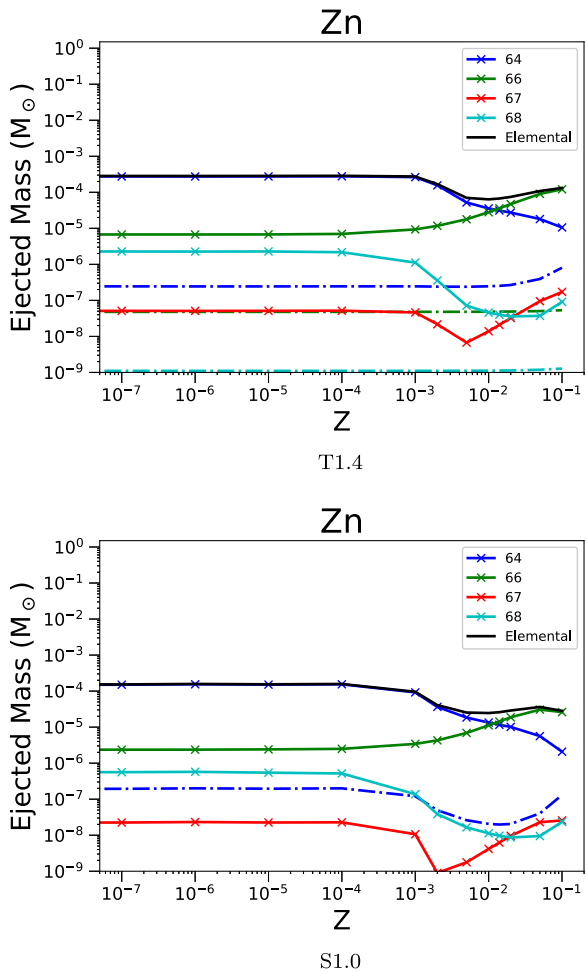
Figure 15. The same as in Figure 4 but for the ejected mass of ^{59}Co.

Figure 16. The same as in Figure 4 but for the ejected mass of Ni, and its stable isotopes ^{58}Ni, ^{60}Ni, ^{61}Ni, ^{62}Ni, and ^{64}Ni.

as ^{68}Ge has become more favorable to produce. In the S1.0 models the nucleosynthesis is similar, with ^{68}Se being the most abundant isotope in the S1.0Z0 models. There is a decrease in the production of ^{68}Se as the initial metallicity increases, and then production becomes dominated by ^{68}Ge, with ^{68}Se produced only in trace amounts.

The decayed yields from the T1.4, S1.0, and M0.8 models are available at Zenodo:Yields (doi:10.5281/zenodo.8060323).

4.13. Metallicity Trends Summary

The isotopes with the largest change in production between $Z_{met} = 0$ and $Z_{met} = 0.1$ for models T1.4, S1.0, and M0.8 are shown in Tables 3, 4, and 5, respectively. We first selected for isotopes with more than a 10^3 increase from $Z_{met} = 0$ to $Z_{met} = 0.1$ from elements with a contribution from SN Ia events as

T1.4

S1.0

Figure 17. The same as in Figure 4 but for the ejected mass of Zn, and its stable isotopes ^{64}Zn, ^{66}Zn, ^{67}Zn, and ^{68}Zn. There is no production of zinc in the M0.8 models, and therefore the plot is omitted.

Table 3
Relative Production in the T1.4 Models for Elements with a Significant Contribution from SN Ia Explosions

Element	Mass	$X_{0.1}/X_0$	$X_{0.1}/X_\odot$
S	34	1.473e+03	7.167e+00
S	36	4.213e+06	3.333e+02
Ar	40	1.104e+05	3.016e+02
Ca	42	2.199e+03	6.060e+00

Note. We present only those isotopes with $X_{0.1}/X_0 > 10^{-3}$ to highlight those isotopes with a strong metallicity dependence. Column 1 shows the change in production between the zero metallicity case and the case with maximum metallicity; column 2 is the same as column 1 but between solar and the maximum metallicity.

Table 4
Relative Production in the S1.0 Models for Elements with a Significant Contribution from SN Ia Explosions

Element	Mass	$X_{0.1}/X_0$	$X_{0.1}/X_\odot$
S	34	3.725e+03	7.600e+00
S	36	7.749e+08	3.118e+02
Ar	38	2.893e+03	7.000e+00
Ar	40	3.582e+08	2.653e+02
Ca	42	1.283e+04	5.408e+00
Ca	46	9.842e+11	5.858e+02
Ca	48	7.955e+17	1.489e+05
Ti	50	1.594e+11	3.477e+01
V	50	6.174e+08	3.148e+01
Cr	54	5.804e+09	1.695e+02
Fe	54	3.281e+03	6.818e+00
Fe	58	2.131e+07	7.692e+01
Ni	64	1.777e+08	1.668e+02

Note. We present only those isotopes with $X_{0.1}/X_0 > 10^{-3}$ to highlight those isotopes with a strong metallicity dependence. Column 1 shows the change in production between the zero metallicity case and maximum metallicity case; column 2 shows that between solar and maximum.

identified in Kobayashi et al. (2020a), and then compared the change in abundances from $Z_{met} = Z_\odot$ to $Z_{met} = 0.1$. We see for the T1.4 case that the isotopes with the largest change in production are from the intermediate-mass region. From the production factors given in Figure 1, we can see that ^{34}S, ^{36}S, ^{40}K, and ^{42}Ca begin to make significant contributions to the solar budget of these isotopes with an initial metallicity close to the solar value. In a similar manner, the S1.0 yields show significant contributions from ^{34}S, ^{38}Ar, ^{40}K, ^{42}Ca, ^{50}V, and ^{54}Cr. While other abundances also increase significantly across the metallicity space, they are in trace amounts. ^{40}Ar may have a significant contribution to solar abundances at supersolar metallicities for S1.0. Metallicity-dependent yields of SN Ia, as well as a well-constrained distribution of the true initial metallicity of SN Ia progenitors and their relative contribution to the solar budget, are therefore vital in determining the origins of ^{34}S, ^{36}S, ^{40}K, and ^{42}Ca in the Chandrasekhar and ^{34}S, ^{38}Ar, ^{40}K, ^{42}Ca, ^{50}V, ^{54}Cr, and, to a lesser extent ^{40}Ar, in the sub-Chandrasekhar cases.

5. Literature Yields Comparisons

In this section, the results of the nucleosynthesis calculations are compared with other yields in the literature, namely Nomoto & Leung (2018) and Seitenzahl et al. (2013b) with the T1.4 models, and Sim et al. (2010) and Gronow et al. (2020)

with the S1.0 models. Results are first compared with their parent model to highlight differences due to the nuclear reaction network.

5.1. Comparison with Parent Models

Shown in Figure 18 is the comparison between our postprocessed models and their parent models from the literature (Townsley et al. 2016; Shen et al. 2018; Miles et al. 2019). For the T1.4 case, we have chosen an ^{22}Ne mass fraction of 0.02, which most closely matches the previously published model. We see that there are some differences, particularly in the heavier iron group region where the ejected mass of Cu is around a factor of 5 less in our postprocessed yields, a factor of 2 for ejected Zn and Ge, and more than an order of magnitude for Ga. Other than these differences, the production in the postprocessed model follows that in the parent model very closely. The smaller ejected masses in the upper iron group are caused by less complete burning, as we see a small increase in the ejected mass of Si, S, Ar, and Ca. Ejected masses for the S1.0Z0.014 model are closer to the parent model than the T1.4Z0.02 case throughout the iron group, with only a significant underproduction of Cu and Zn as compared with the published model, and then by a factor of 2–3. In addition, Mg is also slightly overproduced, and Al and

Table 5
Relative Production in the M0.8 Models for Elements with a Significant
Contribution from SN Ia Explosions

| Element	Mass	$X_{0.1}/X_0$	$X_{0.1}/X_\odot$
S	34	3.379630e+03	6.347826e+00
S	36	9.438503e+08	4.114219e+02
Ar	38	1.733668e+04	6.900000e+00
Ar	40	5.169082e+08	3.635334e+02
Ca	42	2.109705e+04	3.759398e+00
Ca	46	1.066946e+12	5.930233e+02
Ca	48	4.714286e+15	4.400000e+05
Ti	46	3.937107e+04	4.852713e+00
Ti	50	1.183013e+11	1.914894e+01
V	50	4.912621e+08	1.547401e+01
Cr	50	7.035176e+03	1.400000e+01
Cr	54	1.111111e+10	1.681034e+02
Fe	54	5.271318e+03	5.354331e+00
Fe	58	2.083333e+07	7.402423e+01
Ni	62	6.336806e+03	1.196721e+02
Ni	64	1.744898e+11	8.829604e+01
Zn	64	1.140351e+05	3.762663e+01
Zn	66	3.486486e+05	1.425414e+02
Zn	67	1.435374e+03	7.429577e+01

Note. We present only those isotopes with $X_{0.1}/X_0 > 10^{-3}$ to highlight those isotopes with a strong metallicity dependence. Column 1 shows the change in production between the zero metallicity case and maximum metallicity case; column 2 shows that between solar and maximum.

Na are slightly underproduced. Broadly however, the abundances are very close between the two treatments. The same is true for M0.8Z0.014 up to Ni, with only Co underproduced as compared to the parent model, here by around a factor of 5. Cu and Zn, however, are not produced in our postprocessed results, as they are in the parent model, likely due to small increases in the ejected mass of Mg, Al, and P indicating less complete burning than is present in Miles et al. (2019). We conclude that the results of our postprocessing, for the metallicities closest to the parent models, are in each case close to the expected values, with reasonable differences that we attribute to different choices in reaction networks, our treatment of NSE and our choice of a flat ^{22}Ne abundance.

5.2. Comparison with the T1.4 yields

Figure 19 shows the comparison of our T.4Z0.014 model with the W7 yields of Nomoto & Leung (2018; upper panel) and with the N100 model of Seitenzahl et al. (2013b; lower panel). The W7 yields have been updated from the original yields of Nomoto (1982) and later Nomoto et al. (1997b) papers with improved nuclear physics. All models are shown at solar metallicity, which is set in all cases by the initial ^{22}Ne content. The agreement between the models is good, with some differences in the ejected mass of Cl, K, and S where the W7 and Seitenzahl models are enriched by around a factor of 2 compared with the T1.4Z0.014 model. We see that the T1.4Z0.014 model produces more Cu by a factor of around 5, and more Zn by a factor of around 10 than the W7 model. Our agreement with the Seitenzahl yields is generally better than with the W7 model, for example, the Cr/Mn ratio for W7 is < 1 but > 1 for the T1.4Z0.014 and Seitenzahl models.

Nomoto & Leung (2018) used the same 1D structure of the original W7 model; the Townsley et al. (2016) model is 2D; and the Seitenzahl et al. (2013b) models are 3D. For the most
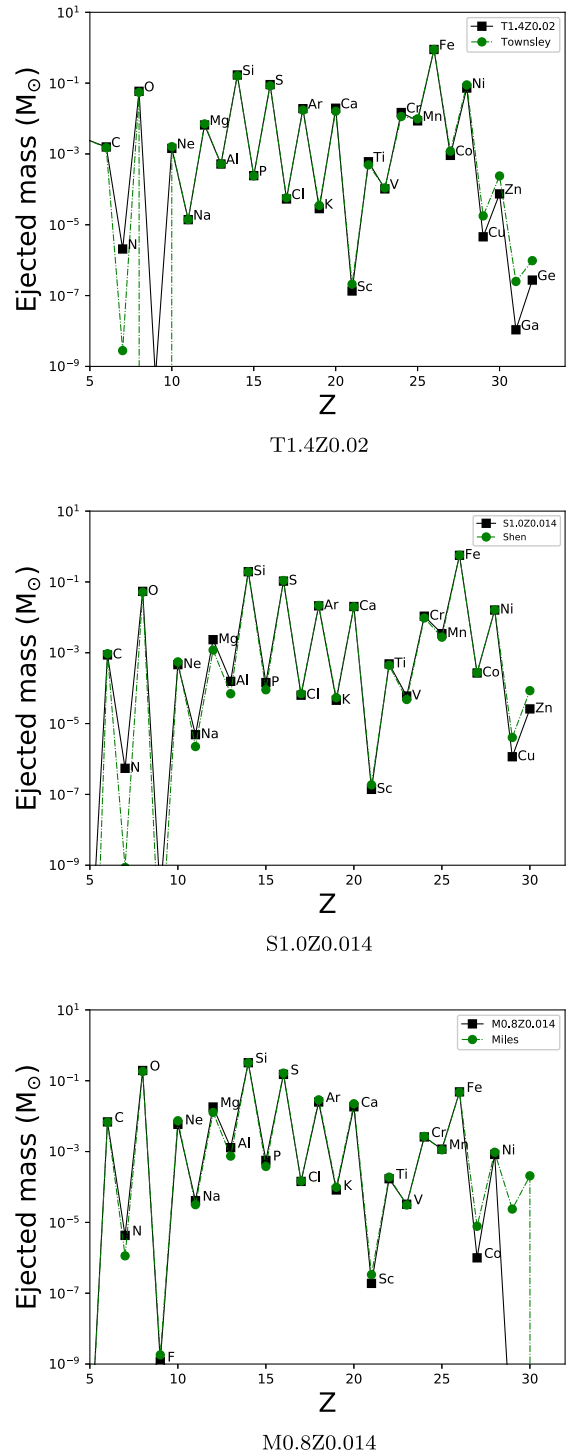
Figure 18. Comparison with the T1.4 yields T1.4Z0.014 (upper panel), S1.0Z0.014 (middle panel), and M0.8Z0.014 (lower panel). In each case, the metallicity closest to the metallicity used in the parent model is selected from our grid of initial ^{22}Ne mass fractions

abundant isotopes, e.g., ^{28}Si, ^{32}S, and ^{56}Fe, the agreement is very good. There is, however, a systematic underproduction of the intermediate-mass, odd-Z elements, as compared with the W7 model. We also see that W7 overproduces Mn as compared with our postprocessed results by a factor of 2, as well as a slightly reduced abundance of Fe leading to a larger [Mn/Fe]. Nomoto & Leung (2018) attributed the relative insensitivity of the Chandrasekhar-mass SN Ia yields to initial metallicity, due
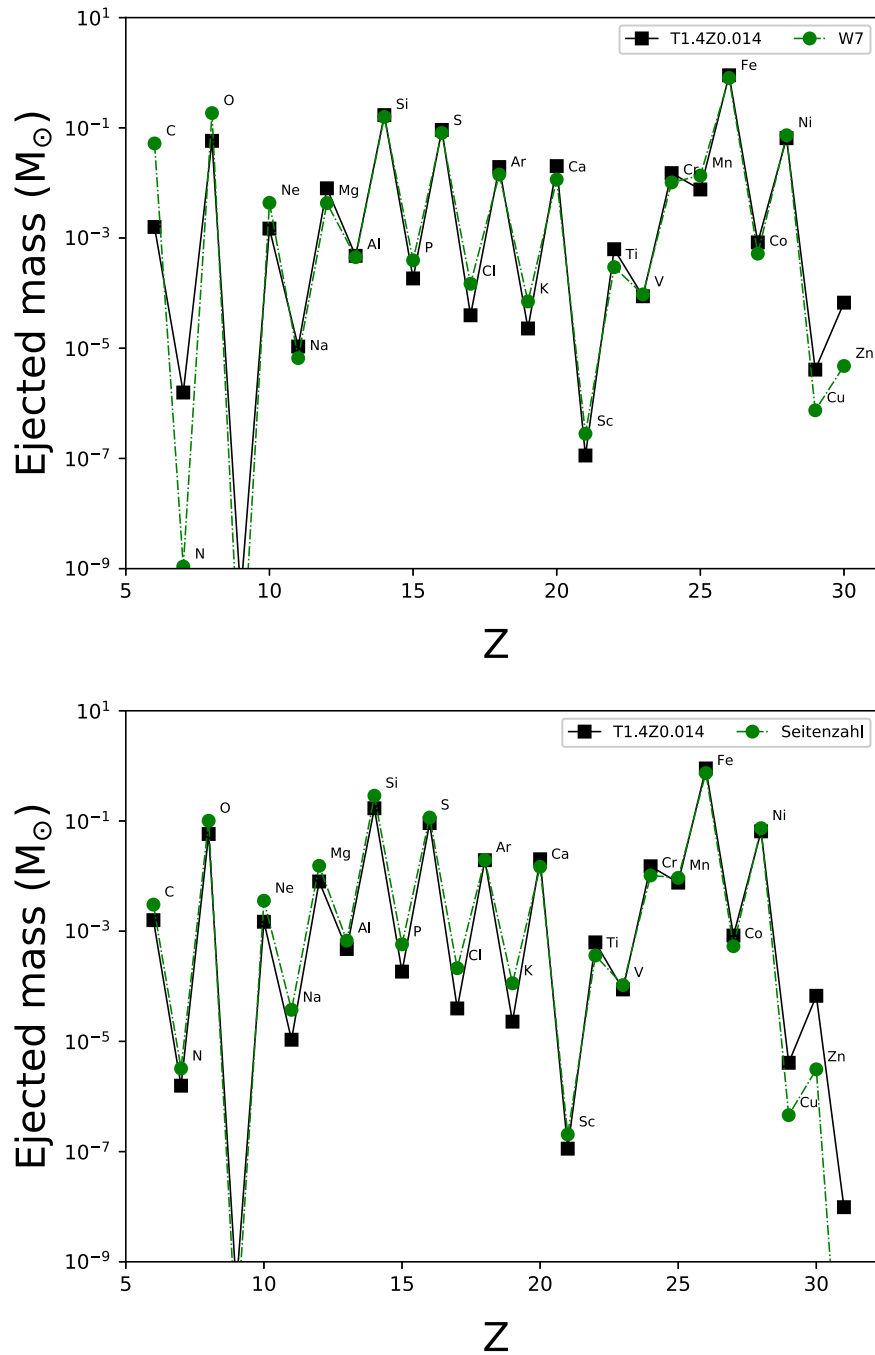
Figure 19. The upper panel shows W7 decayed elemental abundances from Nomoto & Leung (2018; green circles) compared with T1.4Z0.014 (black line, square markers). In the lower panel, the yields from Seitenzahl et al. (2013b) are compared instead.

to the synthesis of neutron-rich isotopes in the hot NSE region. The sensitivity of the outer layers of the WD to the initial metallicity is important, however, as we see a significant metallicity dependence in the intermediate-mass elemental yields.

Note that neither W7 nor Seitenzahl et al. (2013b) produces the trace abundances of Ga and Ge reported in Townsley et al. (2016). The network of Seitenzahl et al. (2013b) contains 384 isotopes, and so is at least as complete as the Townsley et al. (2016) network. This discrepancy is therefore a consequence of the hydrodynamics modeling or the nuclear physics inputs. Zn has a significant ejected mass and is produced in nonnegligible

amounts; however, Ga is over 2 orders of magnitude less abundant than Zn, and is unlikely to have a large effect on the abundances of the iron group through leakage of material above the networks in W7 and Seitenzahl et al. (2013b).

The [Cr/Mn] ratio for our postprocessed models is closer to the value of Seitenzahl et al. (2013b) than to that of the W7 results. Without further study, it is not possible to conclude whether this is due to the hydrodynamical modeling or the differences in reaction networks. More complete burning throughout the T1.4Z0.014 model is indicated by the significantly reduced abundances of C and O.
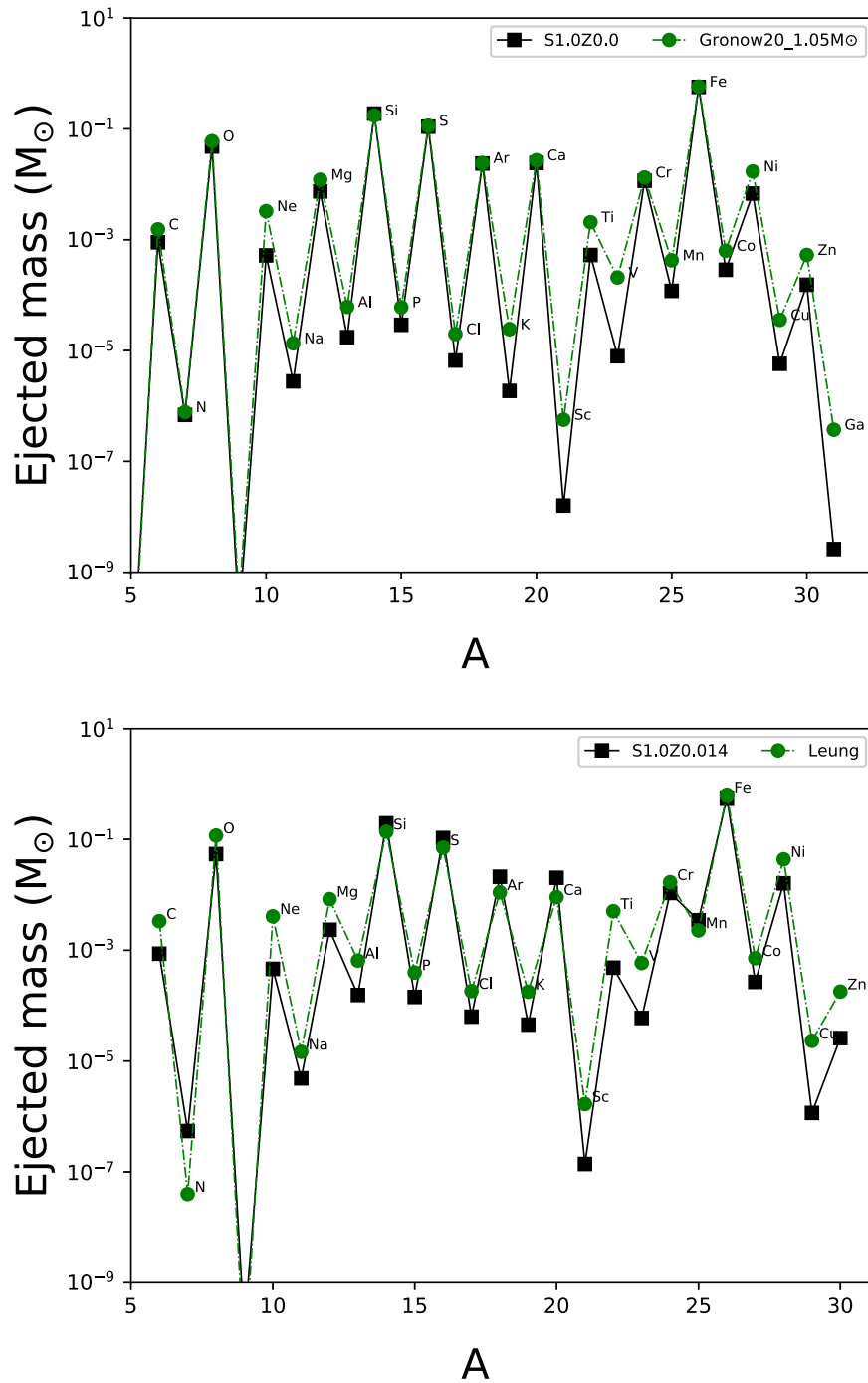
Figure 20. Yields from Gronow et al. (2020, green circles) compared with our S1.0Z0 model (black squares, upper panel), and Leung & Nomoto (2020) compared with model S1.0Z0.014 (lower panel).

5.3. Comparison with the S1.0 Yields

Figure 20 (upper panel) shows a comparison between our postprocessed results for the S1.0Z0 model and the Gronow et al. (2020) SN Ia model. There are some key differences in the model parameters, particularly in the treatment of the accreted helium layer. In the Gronow et al. (2020) work, the helium layer is fully modeled; however, there is a large degree of artificial numerical mixing between the helium layer and the underlying C/O, causing an additional 30%–40% of C/O to be added into the helium layer before the start of the explosion,

which is likely to increase the impact of the helium shell nucleosynthesis significantly.

Further comparison for the 1.0 $M_\odot$ against model Leung & Nomoto (2020) 1.05$M_\odot$ SN Ia are shown in Figure 20, lower panel. C, N, O, F, Si, S, Ar, Cr, Fe, and Co are all within a factor of 2 between the two models. The iron group distribution matches more closely; although the production of Mn in the Shen et al. (2018) postprocessed model is increased by a factor of 15 (Gronow et al. 2020). The detonation mechanism therefore significantly influences the distribution and ejected yields of the SN Ia explosion, both in the iron group region and the intermediate-mass elements. Significant differences in the
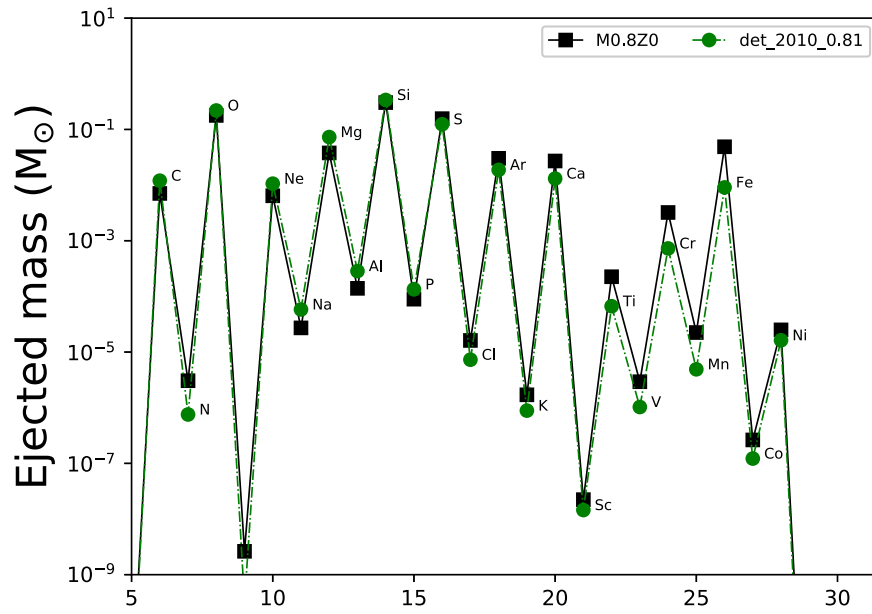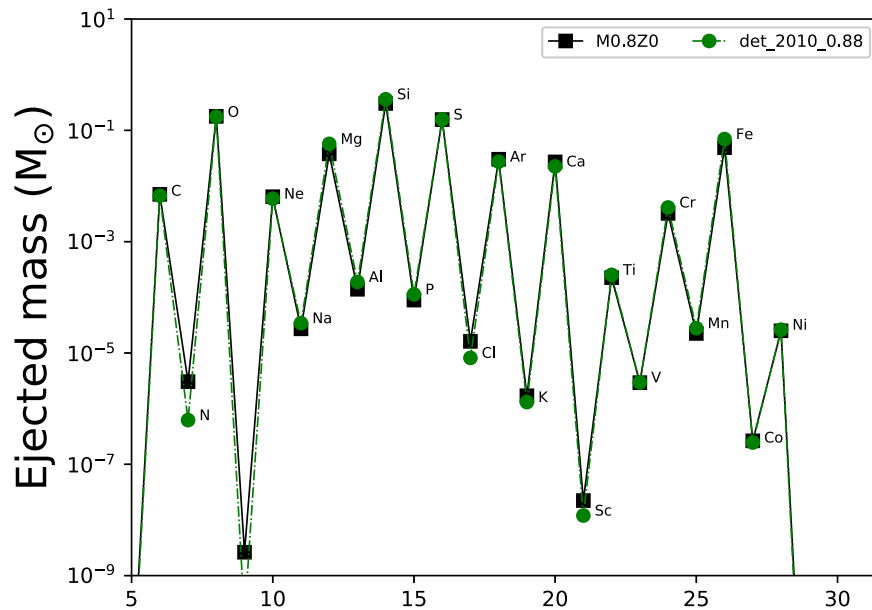
Figure 21. The 0.81 $M_\odot$ model from Sim et al. (2010, green circles) compared with our M0.8Z0 model (black squares, upper panel) and the 0.88 $M_\odot$ model S1.0 from the same publication (lower panel).

abundances of Ti and V are observed, with this postprocessed work being a factor of 5 underproduced compared to that work. A factor of 2 overproduction of the much more abundant Ca accounts for many of the differences. We again see higher production of even Z intermediate-mass elements, and a reduction in the ejected mass of odd-Z intermediate-mass elements as compared with Leung & Nomoto (2020).

In Shen et al. (2018), the helium layer is treated as being minimally thin, and contributing nothing to the ejected mass of the SN Ia. The different treatment of the outer layers of the WD may explain the discrepancies in production of the lower Z

elements (e.g., Al, P, and Cl) as these odd-Z elements are produced primarily in the cooler outer regions of the explosion in the S1.0Z0 model (while the even-Z elements have a larger contribution from the intermediate-temperature regions). A more-massive cooler component may therefore lead to an increase in production, as seen in the Gronow yields; however, as the composition of the He shell is different to the CO core of the S1.0Z0 model, further testing of this result is required. We see a significant increase in the production of elemental Ne, which is again produced in the cool outer regions of the star. Other discrepancies may be due simply to the fact that the

models are of different masses of progenitor, with a difference of $0.05 M_\odot$. For the less abundant species, this will have a large impact. ^{51}V is the largest component of the ejected elemental vanadium and has a broad contribution from ejecta with maximum peak temperatures between 3 and 6 G. Further investigation is needed to determine the origin of this large difference.

5.4. Comparison with the M0.8 Yields

Comparison with the 0.81 and 0.88 $M_\odot$ models of Sim et al. (2010) in Figure 21 show better agreement with the higher-mass model, where only N and Sc differ by a factor of 2 or more. There are larger differences as compared with the 0.81 $M_\odot$ model, where the low Z elements Al, Cl, and K are overproduced in the M0.8Z0 model by around a factor of 2, which may be due to differences in the nuclear network between the runs. It is unclear why the more-massive model more closely matches our results; however, as the yields from all models are consistent, we are satisfied that the parameters of our models are reasonable.

Our 0.8 $M_\odot$ is predicted to be undetectable observationally due to the small mass of ^{56}Ni produced. Sim et al. (2010) showed that their 0.88 $M_\odot$ mass progenitor lies at the limit of observable production of ^{56}Ni—ejecting a total mass of $0.07 M_\odot$ of ^{56}Ni. Their 0.81 $M_\odot$ model ejects a total of $0.01 M_\odot$ of ^{56}Ni, and is not discussed further in their paper due to the absence of a possible observational counterpart. Our M0.8Z0 produces 0.048 $M_\odot$ of ^{56}Ni, close to the observable limit of the 0.88 $M_\odot$ model; however, the observational counterpart of this explosion may not resemble a typical SN Ia explosion.

6. Conclusions

In this work, we have presented yields from 39 models of type Ia supernovae, at three masses (1.4, 1.0, and 0.8 $M_\odot$), and 13 metallicities. The metallicities were varied by changing the ^{22}Ne mass fraction of each tracer particle to a fixed value before postprocessing. In this way, we have investigated the metallicity dependence on the production of all stable isotopes in the SN Ia explosion.

Metallicity dependencies of the ejected elemental yields are negligible in all cases below a mass fraction of ^{22}Ne of 10^{-4}, corresponding to a metallicity $1/100$ that of solar. Significant metallicity effects of a factor of 2 or greater start at a ^{22}Ne mass fraction of around 10^{-3}. Elemental abundances change, in most cases, by a factor of a few; however, for some elements, such as V, with close to monoisotopic contributions, the change in the ejected elemental abundances can be a factor of 5 or 10.

Isotopic abundances are generally more sensitive to the changing ^{22}Ne content, and occur at lower initial ^{22}Ne mass fractions; however, this is a general statement, and each isotope should be considered separately. The impact of a changing initial metallicity is mostly observed in the cooler outer regions of the WD below around 4 GK. There is a limited effect on isotopic distribution in the Chandrasekhar-mass models as electron captures in the high-density central regions cause the electron fraction to converge to a value determined by the central density, washing out the effect of initial composition. Our results agree well with the current literature available for a range of SN Ia masses, and provide much needed metallicity dependence to the available suite of yields.

This work presents a comprehensive suite of models for GCE applications, with a consistent nuclear reaction network between the various masses of model. In this way, we have disentangled the nuclear physics uncertainties from those associated with the explosion models. Further work should focus on fully modeling the accreted helium shell of the double detonation models (S1.0, M0.8), with full realistic abundance distributions. While the effect of seed nuclei in the majority of the CO core will be negligible, due to the same considerations as for the electron fraction, there can be a significant impact on the nucleosynthesis in the cooler layers of the WD, resulting in p-nuclei production. This should be fully investigated in order to accurately describe the contributions of SN Ia to GCE models.

Our models provide an important first step in producing detailed, metallicity-dependent models of SN Ia explosions, which will be used to identify tracers for the sub- to Chandrasekhar-mass progenitor ratio, and identify the burning conditions involved in the production of the full range of SN Ia ejecta. It is noted that, due to the small production of ^{56}Fe in the M0.8 model—with a total ejected mass ranging from 4.87×10^{-2} to 2.32×10^{-2} in mass fraction between $Z_{met} = 0$ to $Z_{met} = 0.1$—the explosion of the M0.8 model would not resemble a standard SN Ia explosion, as the production of ^{56}Ni during the explosion is too small.

ORCID iDs

James D. Keegans ⓘ https://orcid.org/0000-0002-7365-9813
Marco Pignatari ⓘ https://orcid.org/0000-0002-9048-6010
Richard J. Stancliffe ⓘ https://orcid.org/0000-0002-6972-9655
Samuel Jones ⓘ https://orcid.org/0000-0003-3970-1843
Brad K. Gibson ⓘ https://orcid.org/0000-0003-4446-3130
Dean M. Townsley ⓘ https://orcid.org/0000-0002-9538-5948
Broxton J. Miles ⓘ https://orcid.org/0000-0003-1278-2495
Ken J. Shen ⓘ https://orcid.org/0000-0002-9632-6106

References

Angulo, C., Arnould, M., Rayet, M., et al. 1999, NuPhA, 656, 3
Asplund, M., Grevesse, N., Sauval, A. J., & Scott, P. 2009, ARA&A, 47, 481
Bader, G., & Deuflhard, P. 1983, NuMat, 41, 373

Battino, U., Pignatari, M., Travaglio, C., et al. 2020, MNRAS, 497, 4981
Bergemann, M., & Gehren, T. 2008, A&A, 492, 823
Boos, S. J., Townsley, D. M., Shen, K. J., Caldwell, S., & Miles, B. J. 2021, ApJ, 919, 126
Brachwitz, F., Dean, D. J., Hix, W. R., et al. 2000, ApJ, 536, 934
Bravo, E. 2019, A&A, 624, A139
Bravo, E., & Martínez-Pinedo, G. 2012, PhRvC, 85, 055805
Calder, A., Townsley, D., Seitenzahl, I., et al. 2007, ApJ, 656, 313
Cash, J. R., & Karp, A. H. 1990, ACM Trans. Math. Softw., 16, 201
Cassisi, S., Iben, I., Jr, & Tornambè, A. 1998, ApJ, 496, 376
Caughlan, G. R., & Fowler, W. A. 1988, ADNDT, 40, 283
Cescutti, G., & Kobayashi, C. 2017, A&A, 607, A23
Chugunov, A., Dewitt, H., & Yakovlev, D. 2007, PhRvD, 76, 025028
Cyburt, R. H., Amthor, A. M., Ferguson, R., et al. 2010, ApJS, 189, 240
De los Reyes, M. A., Kirby, E. N., Seitenzahl, I. R., & Shen, K. J. 2020, ApJ, 891, 85
Deuflhard, P. 1983, NuMat, 41, 399
Dillmann, I., Heil, M., Käppeler, F., et al. 2006, in AIP Conf. Proc. 819, Capture Gamma-Ray Spectroscopy and Related Topics, ed. A. Woehr & A. Aprahamian (Melville, NY,: AIP), 123
Eitner, P., Bergemann, M., Hansen, C. J., et al. 2020, A&A, 635, A38
Eitner, P., Bergemann, M., Ruiter, A., et al. 2022, arXiv:2206.10258
Fink, M., Röpke, F., Hillebrandt, W., et al. 2010, A&A, 514, A53
Fitzpatrick, T., & Shen, K. J. 2021, arXiv:2112.06951
Flörs, A., Spyromilio, J., Taubenberger, S., et al. 2020, MNRAS, 491, 2902
Foley, R. J., Challis, P. J., Chornock, R., et al. 2013, ApJ, 767, 57
Fryer, C. L., Ruiter, A. J., Belczynski, K., et al. 2010, ApJ, 725, 296
Fryxell, B., Olson, K., Ricker, P., et al. 2000, ApJS, 131, 273
Fuller, G., Fowler, W., & Newman, M. 1985, ApJ, 293, 1
Fuller, G. M., Fowler, W. A., & Newman, M. J. 1982, ApJ, 252, 715
Goriely, S. 1999, A&A, 342, 881
Gronow, S., Collins, C., Ohlmann, S. T., et al. 2020, A&A, 635, A169
Gronow, S., Côté, B., Lach, F., et al. 2021, A&A, 656, A94
Hillebrandt, W., Kromer, M., Röpke, F., & Ruiter, A. 2013, FrPhy, 8, 116
Hillebrandt, W., & Niemeyer, J. C. 2000, ARA&A, 38, 191
Hosseinzadeh, G., Sand, D. J., Valenti, S., et al. 2017, ApJL, 845, L11
Iliadis, C. 2015, Nuclear Physics of Stars (Hoboken, NJ: Wiley)
Iliadis, C., D'Auria, J. M., Starrfield, S., Thompson, W. J., & Wiescher, M. 2001, ApJS, 134, 151
Jones, S., Côté, B., Röpke, F. K., & Wanajo, S. 2019a, ApJ, 882, 170
Jones, S. W., Möller, H., Fryer, C. L., et al. 2019b, MNRAS, 485, 4287
Kahane, C., Dufour, E., Busso, M., et al. 2000, A&A, 357, 669
Kinsey, R., Dunford, C., Tuli, J., & Burrows, T. 1997, in Proc. of the 9th Int. Symp. on Capture Gamma-Ray Spectroscopy and Related Topics, ed. G. Molnar, T. Belgya, & Z. Revay (Berlin: Springer), 657
Kobayashi, C., Karakas, A. I., & Lugaro, M. 2020a, ApJ, 900, 179
Kobayashi, C., Leung, S.-C., & Nomoto, K. 2020b, ApJ, 895, 138
Kobayashi, C., Umeda, H., Nomoto, K., Tominaga, N., & Ohkubo, T. 2006, ApJ, 653, 1145
Kool, E. C., Johansson, J., Sollerman, J., et al. 2023, Natur, 617, 477
Kromer, M., Sim, S., Fink, M., et al. 2010, ApJ, 719, 1067
Lach, F., Roepke, F., Seitenzahl, I., et al. 2020, A&A, 644, A118
Langanke, K., & Martınez-Pinedo, G. 2000, NuPhA, 673, 481
Langanke, K., & Martínez-Pinedo, G. 2001, ADNDT, 79, 1
Lawson, T. V., Pignatari, M., Stancliffe, R. J., et al. 2022, MNRAS, 511, 886
Leung, S.-C., & Nomoto, K. 2018, ApJ, 861, 143
Leung, S.-C., & Nomoto, K. 2020, ApJ, 888, 80
Livio, M., & Mazzali, P. 2018, PhR, 736, 1
Lodders, K. 2003, ApJ, 591, 1220
Magee, M., Maguire, K., Kotak, R., & Sim, S. 2021, MNRAS, 502, 3533
Magkotsios, G., Timmes, F. X., Hungerford, A. L., et al. 2010, ApJS, 191, 66

Maoz, D., & Mannucci, F. 2012, PASA, 29, 447
Maoz, D., Mannucci, F., & Nelemans, G. 2014, ARA&A, 52, 107
Martínez-Rodríguez, H., Badenes, C., Yamaguchi, H., et al. 2017, ApJ, 843, 35
Matteucci, F. 2021, A&ARv, 29, 5
Matteucci, F., & Greggio, L. 1986, A&A, 154, 279
Matteucci, F., Spitoni, E., Recchi, S., & Valiante, R. 2009, A&A, 501, 531
Mennekens, N., Vanbeveren, D., De Greve, J., & De Donder, E. 2010, A&A, 515, A89
Miles, B. J., Townsley, D. M., Shen, K. J., Timmes, F., & Moore, K. 2019, ApJ, 871, 154
Mishenina, T., Gorbaneva, T., Pignatari, M., Thielemann, F.-K., & Korotin, S. 2015, MNRAS, 454, 1585
Mishenina, T., Pignatari, M., Côté, B., et al. 2017, MNRAS, 469, 4378
Nomoto, K. 1982, ApJ, 257, 780
Nomoto, K., Iwamoto, K., & Kishimoto, N. 1997a, Sci, 276, 1378
Nomoto, K., Iwamoto, K., Nakasato, N., et al. 1997b, NuPhA, 621, 467
Nomoto, K., & Leung, S.-C. 2017, in Handbook of Supernovae, ed. A. Alsabti & P. Murdin (New York: Springer), 1275
Nomoto, K., & Leung, S.-C. 2018, SSRv, 214, 67
Nomoto, K., Thielemann, F.-K., & Yokoi, K. 1984, ApJ, 286, 644
Oda, T., Hino, M., Muto, K., Takahara, M., & Sato, K. 1994, ADNDT, 56, 231
Pakmor, R., Kromer, M., Röpke, F. K., et al. 2010, Natur, 463, 61
Parikh, A., José, J., Seitenzahl, I. R., & Röpke, F. K. 2013, A&A, 557, A3
Paxton, B., Bildsten, L., Dotter, A., et al. 2010, ApJS, 192, 3
Pignatari, M., Gallino, R., Heil, M., et al. 2010, ApJ, 710, 1557
Pignatari, M., Herwig, F., Hirschi, R., et al. 2016, ApJS, 225, 24
Pignatari, M., Hoppe, P., Trappitsch, R., et al. 2018, GeCoA, 221, 37
Prantzos, N., Abia, C., Limongi, M., Chieffi, A., & Cristallo, S. 2018, MNRAS, 476, 3432
Raskin, C., Scannapieco, E., Rockefeller, G., et al. 2010, ApJ, 724, 111
Rauscher, T., Heger, A., Hoffman, R. D., & Woosley, S. E. 2002, ApJ, 576, 323
Rauscher, T., & Thielemann, F.-K. 2000, ADNDT, 75, 1
Ritter, C., Herwig, F., Jones, S., et al. 2018, MNRAS, 480, 538
Scalzo, R., Ruiter, A., & Sim, S. 2014, MNRAS, 445, 2535
Seitenzahl, I., Timmes, F., Marin-Laflèche, A., et al. 2008, ApJL, 685, L129
Seitenzahl, I. R., Cescutti, G., Röpke, F. K., Ruiter, A. J., & Pakmor, R. 2013a, A&A, 559, L5
Seitenzahl, I. R., Ciaraldi-Schoolmann, F., Röpke, F. K., et al. 2013b, MNRAS, 429, 1156
Shen, K. J., Kasen, D., Miles, B. J., & Townsley, D. M. 2018, ApJ, 854, 52
Silverman, J. M., Vinkó, J., Marion, G., et al. 2015, MNRAS, 451, 1973
Sim, S., Röpke, F., Hillebrandt, W., et al. 2010, ApJL, 714, L52
Summa, A., Ulyanov, A., Kromer, M., et al. 2013, A&A, 554, A67
Takahashi, K., & Yokoi, K. 1987, ADNDT, 36, 375
The, L.-S., El Eid, M. F., & Meyer, B. S. 2007, ApJ, 655, 1058
Timmes, F. 1999, ApJS, 124, 241
Timmes, F. X., Brown, E. F., & Truran, J. 2003, ApJL, 590, L83
Townsley, D. M., Calder, A., Asida, S., et al. 2007, ApJ, 668, 1118
Townsley, D. M., Miles, B. J., Timmes, F., Calder, A. C., & Brown, E. F. 2016, ApJS, 225, 3
Travaglio, C., Gallino, R., Rauscher, T., Röpke, F. K., & Hillebrandt, W. 2015, ApJ, 799, 54
Travaglio, C., Hillebrandt, W., & Reinecke, M. 2005, A&A, 443, 1007
Travaglio, C., Hillebrandt, W., Reinecke, M., & Thielemann, F.-K. 2004, A&A, 425, 1029
Travaglio, C., Röpke, F., Gallino, R., & Hillebrandt, W. 2011, ApJ, 739, 93
Truran, J. W., Arnett, W. D., & Cameron, A. G. W. 1967, CaJPh, 45, 2315
Woods, T. E., & Gilfanov, M. 2014, Ap&SS, 354, 69
Woosley, S. E., Heger, A., & Weaver, T. A. 2002, RvMP, 74, 1015